Nonautonomous spectral submanifolds for model reduction of nonlinear mechanical systems under parametric resonance

Thurnher, Thomas; Haller, George; Jain, Shobhit

Important note
To cite this publication, please use the final published version (if applicable).
Please check the document version above.

Nonautonomous spectral submanifolds for model reduction of nonlinear mechanical systems under parametric resonance

Special Collection: Nonlinear Model Reduction From Equations and Data

Thomas Thurnher (iD) ; George Haller (iD) ; Shobhit Jain ✉ (iD)

Check for updates

View Online

Export Citation

Chaos

Focus Issue:

Intelligent Game on Networked Systems: Optimization, Evolution and Control

Guest Editors: Lin Wang, Yang Lou, Zhihai Rong, and Guanrong Chen

Submit Today!

AIP Publishing

AIP Publishing

Nonautonomous spectral submanifolds for model reduction of nonlinear mechanical systems under parametric resonance

View Online   Export Citation   CrossMark

Thomas Thurnher,[1] George Haller,[1] and Shobhit Jain[2,a]

AFFILIATIONS

[1] Institute for Mechanical Systems, ETH Zürich, Leonhardstrasse 21, 8092 Zürich, Switzerland
[2] Delft Institute of Applied Mathematics, TU Delft, Mekelweg 4, 2628 CD Delft, The Netherlands

Note: This paper is part of the Focus Issue on Nonlinear Model Reduction From Equations and Data.
[a] **Author to whom correspondence should be addressed:** Shobhit.Jain@tudelft.nl

ABSTRACT

We use the recent theory of spectral submanifolds (SSMs) for model reduction of nonlinear mechanical systems subject to parametric excitations. Specifically, we develop expressions for higher-order nonautonomous terms in the parameterization of SSMs and their reduced dynamics. We provide these results for both general first-order and second-order mechanical systems under periodic and quasiperiodic excitation using a multi-index based approach, thereby optimizing memory requirements and the computational procedure. We further provide theoretical results that simplify the SSM parametrization for general second-order dynamical systems. More practically, we show how the reduced dynamics on the SSM can be used to extract the resonance tongues and the forced response around the principal resonances in parametrically excited systems. In the case of two-dimensional SSMs, we formulate explicit expressions for computing the steady-state response as the zero-level set of a two-dimensional function for systems that are subject to external as well as parametric excitation. This allows us to parallelize the computation of the forced response over the range of excitation frequencies. We demonstrate our results on several examples of varying complexity, including finite-element-type examples of mechanical systems. Furthermore, we provide an open-source implementation of all these results in the software package `SSMTool`.

As the complexity of engineering systems, such as MEMS devices, is growing, accurate reduced-order models (ROMs) are in high demand. Not only do such models promise quick routines for system design and analysis, but they can also deliver specifically desired information that might be inaccessible from a full-system simulation. Reduction of the full system to spectral submanifolds (SSMs) offers a rigorous mathematical procedure to derive such ROMs for nonlinear systems. In this paper, we develop a methodology for computing nonautonomous approximations to these SSMs up to arbitrary order, generalizing, improving, and expanding available results in the literature. Using the exact ROM provided by the SSM-reduced dynamics, we analyze instabilities that arise due to parametric resonance and obtain the resulting steady states for a number of examples. Our results are also implemented in an open-source software library.

I. INTRODUCTION

Parametric excitation refers to forcing on a mechanical system that arises from the time dependence of its parameters, rather than from an external effect. This time dependence may be due to modulation of physical parameters or due to inherent nonlinear couplings.[1] Perhaps, the simplest example is the periodic modulation of the length of a pendulum that may even destabilize its stable fixed point. This phenomenon is known as parametric resonance and occurs if the modulation frequency and the eigenfrequency of the pendulum assume a rational relationship.

Due to its destabilizing effect, parametric resonance is often avoided in the operational regime of engineering systems.[2,3] However, it is also possible to take advantage of the resulting instability, which leads to exponential growth of energy and oscillation amplitudes. In rotor dynamics, for instance, parametric resonance may

22 July 2024 13:58:33

be used to virtually increase damping.[4] Nonlinear energy harvesters show increased performance when driven in the regime of parametric resonance compared to systems using conventional resonance.[5] Micro-electromechanical systems (MEMS) also frequently make use of parametric resonance. Examples include low-noise parametric amplifiers,[6] mass-sensing devices,[7] signal amplifiers,[8] gyroscopes,[9,10] picoprojectors, and microscanners.[11] Parametric resonance in combination with nonlinearities can also enable operation in a wider frequency range.[12]

Among various types of parametric resonances, the *principal parametric resonance*, where the external excitation frequency Ω and a system's modal frequency ω_i obey a relation of the form $\Omega = 2\omega_i$, is of pronounced practical interest. Indeed, due to the presence of damping, higher-order parametric resonances become effectively inaccessible in most engineering structures.[1,11,13,14] Nonetheless, high-order parametric resonances have been observed in specially engineered systems.[15,16]

A. Forced response curves

Forced response curves (FRCs) visualize the relationship between a system's response amplitude and its excitation frequency. FRCs provide insights into the nonlinear characteristics of a system when compared to the linear frequency response, especially near resonance. Various techniques have been used to analyze parametrically excited systems. For instance, the Poincaré–Lindstedt method assumes the dependence of the period of the solution on a small excitation amplitude and expresses the periodic solution as an asymptotic series for weakly excited systems.[17] The method of multiple scales introduces different temporal variables for different timescales. These are then used in perturbation expansions and can be applied to parametrically excited systems as well.[18] Other common methods found in the parametric excitation literature are averaging[6,9,19–21] and the analytical construction of approximate solutions, for instance, using a harmonic series[22–25] or direct numerical simulation.[26]

For a systematic computation of FRCs, numerical continuation packages, such as AUTO,[27] COCO,[28] MATCONT,[29] LOCA[30] or the harmonic balance-based manlab,[31] and NLvib,[32] may be used. These methods are based on collocation or spectral discretization and enable a global approximation of the nonlinear periodic solution. However, when applied to the full system for computing FRCs in high-dimensional finite-element models, these methods have been reported to carry prohibitively high computational costs in the available literature.[33–36]

B. Stability diagrams

Establishing the stability type of trivial fixed points is the first important step in the study of parametrically excited systems. The regions of instability and stability of these fixed points are plotted in an excitation amplitude vs frequency diagram, often referred to as *Strutt* or *Ince Strutt* diagram. In these stability diagrams, the regions of instability are often called *Floquet tongues* that extend in the direction of decreasing forcing amplitude as the system's damping decreases. The simplest technique for constructing stability diagrams is numerical time integration over a grid of amplitude and

frequency parameters.[8] More sophisticated approaches employ Floquet theory and range from the method of infinite determinants in the conservative case[37] to spectral methods for obtaining the eigenvalues of the monodromy matrix.[8,37,38] In the extended phase space, a bifurcation of the trivial periodic orbits occurs along the stability boundary, which enables its computation using continuation techniques.[1]

C. Model reduction

The methods discussed above are well suited for computing FRCs and stability diagrams in low-dimensional examples under parametric excitation. For the analysis of realistic high-dimensional systems, however, reduced-order models (ROMs) are necessary. While projection onto modal subspaces is a powerful ROM technique for linear systems, in nonlinear systems, those subspaces lose their invariance. The dynamics and the trajectories projected on them, thus, no longer correspond to those of the full dynamical system.

In contrast, nonlinear normal modes (NNMs)[39] are invariant manifolds that perturb from linear modal subspaces and serve as the nonlinear analogs of those subspaces. Using projections to NNMs, Warminski et al.[40] analyzed parametrically and externally excited mechanical systems. Sinha et al.[41,42] employed Lyapunov–Floquet transformations to parametrically forced systems to obtain systems with autonomous linear part before computing NNMs. However, this method[41,42] is feasible only for low-dimensional systems because of its reliance on the initial transformation.

Furthermore, the existence and uniqueness of such NNMs is *a priori* unclear. Indeed, NNMs are an important subclass of invariant manifolds that were formally computed using Taylor expansions in the seminal work of Shaw and Pierre.[39,43] It should be noted, however, that several classes of invariant manifolds relevant for model reduction may be disjoint from NNMs, e.g., fractionally smooth invariant manifolds, which cannot be captured by Taylor expansions and are nonunique.[44] The fact that the smoothest NNMs can be captured uniquely via Taylor expansions was established due to the important theoretical contributions of De la Llave and co-workers.[45–48] This unique smoothest NNM is also called the primary spectral submanifold (SSM).[44,49] As we only focus on the computation of primary SSMs in this work, we will refer to primary SSMs simply as SSMs for brevity.

Specifically, an SSM is the unique smoothest invariant manifold that perturbs from a modal subspace under the addition of nonlinearities and small-amplitude parametric or external forcing. The existence and uniqueness of an SSM are guaranteed under appropriate non-resonance conditions.[49] SSMs associated with slow eigenspaces (slow SSMs) attract nearby trajectories of the full system. Hence, the reduced dynamics on an SSM serves as a locally exact, nonlinear reduced-order model for the full system.[50,51]

In recent years, significant advances have been made toward the automated computation of SSMs. In a first implementation, Ponsioen et al.[52] proposed a routine for the automated computation of two-dimensional SSMs in modal coordinates. More recent efforts have focused on multidimensional SSM computation in physical coordinates, using only the eigenvectors associated with the master modal subspace.[34,53] This alleviated the computational burden

imposed by a modal transformation and enabled SSM computations for high-dimensional finite-element models.

In particular, for systems without internal resonances, the reduced dynamics on two-dimensional SSMs have been used to compute the forced response of periodically excited nonlinear systems without any numerical simulation, simply by finding the zero-level set of a function.[54] Coupled with the automated SSM computation procedure, this makes the extraction of FRCs very fast for high-dimensional finite-element problems as well.[34] If internal resonances are present, SSMs of higher dimension need to be computed over the linear modes involved in the resonance.[35,53,55] More recently, SSMs have also been constructed directly from individual trajectory data,[56] used in control theory[57,58] and for systems with algebraic constraints.[59] All these developments, however, used only a leading-order approximation for the nonautonomous terms in the SSM and its reduced dynamics.

To capture parametric effects, a high-order approximation of non-autonomous SSMs and their reduced dynamics is necessary. Ponsioen *et al.*[60] have already presented such higher-order computations of the non-autonomous SSM, albeit in modal coordinates. For efficient memory management and for avoiding redundant computations, they employ a multi-index notation in their numerical algorithm. More recently, Opreni *et al.*[61] have developed expressions for the computation of nonautonomous SSMs in physical coordinates for systems with proportional damping and geometric nonlinearities up to cubic order. Their expressions enable the analysis of various mechanical systems subject to an external periodic excitation, but without any explicit parametric forcing.

D. Our contributions

In this work, we consider mechanical systems with general damping and geometric/material nonlinearities of arbitrary polynomial order subject to external as well as parametric excitation (see Sec. II). Extending prior developments[34,35,53,55,61] to enable the treatment of parametric excitations, we develop here expressions for automated computation of non-autonomous SSMs and their reduced dynamics in physical coordinates (see Secs. III and IV). We also develop similar expressions for general first-order dynamical systems in Appendix A 3. Although our applications focus on periodically excited systems, our expressions and their numerical implementations are developed for the general quasiperiodic case and are openly available in the software package SSMTool 2.4.[62]

For the case of two-dimensional periodic SSMs, we develop the following results.

1. *Stability diagrams of parametrically excited systems*: We demonstrate how SSM theory can be used to obtain stability diagrams for the principal parametric resonance of finite-element examples directly from the ROM. Additionally, we analyze the forced response arising from these instabilities using the reduced dynamics on the SSM. We provide an automated routine for the extraction of these stability diagrams in Sec. V along with numerical examples.

2. *Forced response under parametric resonance*: We show how the FRCs of mechanical systems subject to external as well as parametric periodic excitation can be obtained using an analytic transformation of the reduced dynamics on the SSM, without

the need for any numerical continuation (see Lemma 5). This result allows for parallelization of the FRC computation over any desired frequency range, as we demonstrate in Sec. VI.

In addition to the primary contributions mentioned above, we present the following secondary insights in this work.

(a) Computational benefits for general second-order systems: In prior work,[53,61] a special structure in the invariance equations was exploited to reduce the number of equations in SSM computation for second-order mechanical systems containing up to cubic-order geometric nonlinearity and proportional damping. We show how these advantages carry over to SSM computations for general second-order dynamical systems (see Lemmas 1–4 and Remark 3).

(b) Multi-index notation: We use the classic multi-index notation (see, e.g., Haro *et al.*[48]) for developing our expressions instead of the tensor or the indicial notation commonly used in mechanics computations.[34,53,61] We discuss how the multi-index notation minimizes the memory requirements and the number of equations that need to be solved at each polynomial degree (see Appendix A 1 b).

II. SETUP

We consider a quasiperiodically forced nonlinear mechanical system of dimension n.

$$M\ddot{y} + C\dot{y} + Ky + f(y, \dot{y}) = \varepsilon g(\Omega t, y, \dot{y}), \quad 0 \leq \varepsilon \ll 1, \quad (1)$$

with $y \in \mathbb{R}^n$ being the generalized displacement and $M, C, K \in \mathbb{R}^{n \times n}$ denoting the mass, damping, and stiffness matrices, respectively. The function $f(y, \dot{y})$ is a nonlinear function that is r times continuously differentiable with $r \geq 1$. We allow two types of forces to be included in the general excitation function $g(\Omega t, y, \dot{y})$ with the frequency vector $\Omega \in \mathbb{R}^K$ for some $K \geq 0$, i.e.,

$$g(\Omega t, y, \dot{y}) = f_{\text{ext}}(\Omega t) + f_{\text{param}}(\Omega t, y, \dot{y}), \quad (2)$$

where g will be autonomous for $K = 0$, periodic in t for $K = 1$, and quasiperiodic in t for $K > 1$ with K rationally incommensurate frequencies. We note that parametric forcing involves time variation of system parameters, which manifests in the equations of motion as terms with combined state and time dependence. Accordingly, we allow for parametric excitation via $f_{\text{param}}(\Omega t, y, \dot{y})$ and possibly also external forcing via $f_{\text{ext}}(\Omega t)$. Here, f_{param} is a general function of y and $\dot{y}$ and is taken to be C^r in these variables.

The second-order system (1) can be transformed to the first-order form

$$B\dot{z} = Az + F(z) + \varepsilon G(\Omega t, z), \quad (3)$$

where

$$z = \begin{bmatrix} y \\ \dot{y} \end{bmatrix}, A = \begin{bmatrix} -K & 0 \\ 0 & M \end{bmatrix}, B = \begin{bmatrix} C & M \\ M & 0 \end{bmatrix}, \quad (4)$$

$$F(z) = \begin{bmatrix} -f(y, \dot{y}) \\ 0 \end{bmatrix}, G(\Omega t, z) = \begin{bmatrix} g(\Omega t, y, \dot{y}) \\ 0 \end{bmatrix}, \quad (5)$$

with $z \in \mathbb{R}^N, N = 2n$. This choice for the first-order form is not unique[34] but all such forms can be used for the computation of SSMs.

The autonomous linear part of system (3),

$$B\dot{z} = Az, \tag{6}$$

has a fixed point at $z = 0$, which we assume to be hyperbolic and stable. We focus on an even subset of $M \ll N$ eigenvalues and eigenvectors of system (6), the choice of which is discussed below. Note that the task of finding specific subsets of eigenvalues and eigenvectors can be carried out efficiently with iterative algorithms, as presented, for instance, by Golub and Van Loan.[63]

The reduced left and right eigenvalue problems are given by

$$(A - \lambda_j B)v_j = 0, \quad u_j^*(A - \lambda_j B) = 0, \tag{7}$$

$$(A - \overline{\lambda_j} B)\overline{v_j} = 0, \quad \overline{u_j^*}(A - \overline{\lambda_j} B) = 0, \tag{8}$$

for $j = 1, \ldots, M/2$. We arrange these eigenvectors in the increasing order of magnitudes of the real parts of the associated eigenvalues, i.e.,

$$\mathrm{Re}(\lambda_{M/2}) \le \mathrm{Re}(\lambda_{M/2-1}) \le \cdots \le \mathrm{Re}(\lambda_1) < 0. \tag{9}$$

The choice of A and B in Eq. (4) results in displacement and velocity variables that are inherently related, such that

$$v_j = \begin{bmatrix} \phi_j \\ \phi_j \lambda_j \end{bmatrix}, \; u_j = \begin{bmatrix} \theta_j \\ \theta_j \overline{\lambda_j} \end{bmatrix}, \tag{10}$$

$$\overline{v_j} = \begin{bmatrix} \overline{\phi_j} \\ \overline{\phi_j} \lambda_j \end{bmatrix}, \; \overline{u_j} = \begin{bmatrix} \overline{\theta_j} \\ \overline{\theta_j} \lambda_j \end{bmatrix}, \tag{11}$$

where the vectors $\phi_j, \theta_j \in \mathbb{C}^n$ are the right and left eigenvectors associated with the quadratic eigenvalue problem

$$(\lambda_j^2 M + \lambda_j C + K)\phi_j = 0, \quad \theta_j^*(\lambda_j^2 M + \lambda_j C + K) = 0, \tag{12}$$

$$(\overline{\lambda_j^2} M + \overline{\lambda_j} C + K)\overline{\phi_j} = 0, \quad \overline{\theta_j^*}(\overline{\lambda_j^2} M + \overline{\lambda_j} C + K) = 0, \tag{13}$$

for $j = 1, \ldots, M/2$.

Note that the above procedure is valid for any general damping matrix C and reduces to the computation of conservative eigenmodes when C is simultaneously diagonalizable with the mass and stiffness matrices, e.g., in the case of proportional damping.

III. NON-AUTONOMOUS SSMs AND MODEL REDUCTION

Spectral submanifolds (SSMs) are the unique, smoothest continuations of non-resonant spectral subspaces, as defined in Ref. 49. These SSMs are as smooth as the original dynamical system. Infinitely many additional invariant manifolds of the same dimension but of strictly lower smoothness class co-exist with SSMs and are also tangent to the same spectral subspace as the SSMs are (see Ref. 44). An optimal upper bound on the smoothness of these secondary (or fractional) submanifolds is given by the spectral quotient (introduced by Ref. 49), which is computable from the linearized spectrum. However, the determination of the spectral quotient is not necessary for approximating the unique (primary) SSMs up to any desired order. Indeed, by Ref. 49, primary SSMs are known to be of

class C^∞ for C^∞ finite-element problems, such as those considered here.

We now introduce the methodology for computing the SSMs on which the ROM of the parametrically excited system (1) is constructed. The complex–conjugate pairs of right eigenvectors span the spectral subspaces $E_j = \mathrm{span}\{v_j, \overline{v_j}\}$, which are invariant under the linear flow of system (6). To analyze the linear system response via a ROM, we select a M-dimensional spectral subspace $\mathcal{E} = E_1 \oplus E_2 \oplus \cdots \oplus E_{M/2}$, the *master spectral subspace*. The modes E_j are chosen such that the corresponding spectrum

$$\mathrm{Spec}(\mathcal{E}) = \{\lambda_1, \overline{\lambda_1} \cdots, \lambda_{M/2}, \overline{\lambda_{M/2}}\} \tag{14}$$

contains pairs of eigenvalues that potentially assume near-resonance relationships with either the forcing frequencies or among each other. In the absence of any (near) resonances, the subspace $\mathcal{E}$ typically contains the slowest modes of the system. The corresponding eigenvectors are normalized such that

$$(u_i)^* B v_j = \delta_{ij}, \tag{15}$$

which implies $\theta_i^* C \phi_j + \lambda_i \theta_i^* M \phi_j + \lambda_j \theta_j^* M \phi_i = \delta_{ij}$. Note that this normalization choice is different from the commonly adopted mass normalization for proportionally damped systems, i.e., $\phi_i^* M \phi_j = \delta_{ij}$.

Under the addition of nonlinearities to system (6), the subspace $\mathcal{E}$ does not remain invariant. Model reduction onto $\mathcal{E}$ then loses its justification as the trajectories projected onto $\mathcal{E}$ no longer correspond to the trajectories of the full dynamical system. A mathematically rigorous alternative is to construct an invariant manifold that acts as a nonlinear continuation of $\mathcal{E}$. *Spectral submanifolds* (SSMs)[49] are such continuations with their existence conditioned on a set of resonance conditions.[60] Specifically, an *autonomous* SSM, $\mathscr{W}(\mathcal{E})$, is the unique smoothest invariant manifold that perturbs smoothly from the spectral subspace $\mathcal{E}$ under the addition of the nonlinear autonomous terms $f(x, \dot{x})$ to the linearized dynamical system (6). The dynamics of such an SSM are called its *reduced dynamics* and serve as an exact ROM of the full dynamical system (1) for $\varepsilon = 0$.

Under the addition of quasiperiodic excitation (i.e., for $\varepsilon > 0$, small), this autonomous manifold starts to oscillate and deform, becoming a *non-autonomous* SSM, $\mathscr{W}_{\gamma_\varepsilon}(\mathcal{E})$. Instead of being anchored to the trivial fixed point $z = 0$, the quasiperiodic SSM is now attached to $\mathscr{O}(\varepsilon)$ C^r-close invariant torus γ_ε into which this fixed point perturbs.[64] The tangency of the autonomous SSM to $\mathcal{E}$ implies that the nonautonomous SSM perturbs from the spectral subbundle $\gamma_\varepsilon \times \mathcal{E}$. Now, we will use

$$\phi = \Omega t \in \mathbb{T}^K$$

to denote the phase of the quasiperiodic excitation term. For computing $\mathscr{W}_{\gamma_\varepsilon}(\mathcal{E})$ and its reduced dynamics, the following results are useful.[49]

1. $\mathscr{W}_{\gamma_\varepsilon}(\mathcal{E})$ can be described by a time dependent parametrization

$$W_\varepsilon(p, \phi) : \mathcal{U} = U \times \mathbb{T}^K \mapsto \mathbb{R}^N, \quad U \in \mathbb{C}^M, \tag{16}$$

from an open set $\mathscr{U}$ onto the phase space of the full system (3).

2. The reduced vector field $R_\varepsilon(p, \phi) : \mathscr{U} \times \mathbb{T}^K \mapsto \mathscr{U}$ on $\mathscr{W}_{\gamma_\varepsilon}(\mathscr{E})$ satisfies the *invariance equation*

$$B((\partial_p W_\varepsilon)R_\varepsilon + (\partial_\phi W_\varepsilon)\Omega) = A W_\varepsilon + F \circ W_\varepsilon + \varepsilon G(\phi, W_\varepsilon) \quad (17)$$

and generates the reduced dynamics on $\mathscr{W}_{\gamma_\varepsilon}(\mathscr{E})$ via the ordinary differential equation (ODE),

$$\dot{p} = R_\varepsilon(p, \phi), \quad \dot{\phi} = \Omega. \quad (18)$$

If for a given dynamical system we wish to obtain a mathematically exact ROM, it is therefore our task to try and construct representations of the SSM parametrization W_ε and the reduced vector field R_ε. Once this has been achieved, the low-dimensional reduced dynamics can be analyzed in detail. Due to the invariance of the SSM $\mathscr{W}_{\gamma_\varepsilon}(\mathscr{E})$, any periodic orbit, invariant torus, and bifurcation that is observed in Eq. (18) also exists in the full system and can be mapped back using the SSM parametrization W_ε to the full system (1).

IV. SSM COMPUTATION

In this section, we address how the SSM parametrization W_ε and the reduced vector field R_ε can be efficiently computed up to arbitrary orders of accuracy for general mechanical systems. We will merely require knowledge of the eigenvectors and eigenvalues of the underlying master modal subspace over which the SSM is constructed. All computations will be carried out in physical coordinates, without the need of a modal transformation. This will enable the treatment of large dynamical systems arising, e.g., from finite-element models.

A. SSM parametrization

For a second-order system, the phase space variables $z = (y, \dot{y})^T$ are inherently connected as the velocity components are simply the time derivative of the displacement variables. Naturally, this relationship carries over to the SSM parametrization $W_\varepsilon(p, \phi)$, which maps to the phase space. This allows us to express the SSM parametrization as

$$W_\varepsilon(p, \phi) = \begin{bmatrix} w_\varepsilon(p, \phi) \\ \dot{w}_\varepsilon(p, \phi) \end{bmatrix}, \quad (19)$$

where w_ε and $\dot{w}_\varepsilon$ denote the parametrizations for the displacement and the velocity variables. The smooth dependence of the SSM $\mathscr{W}_{\gamma_\varepsilon}(\mathscr{E})$ on ε allows us to further expand these parametrizations in ε as

$$W_\varepsilon(p, \phi) = W(p) + \varepsilon X(p, \phi) + \cdots \quad (20)$$

$$= \begin{bmatrix} w(p) \\ \dot{w}(p) \end{bmatrix} + \varepsilon \begin{bmatrix} x(p, \phi) \\ \dot{x}(p, \phi) \end{bmatrix} + \cdots. \quad (21)$$

Similarly, we expand the reduced dynamics parametrization as

$$R_\varepsilon(p, \phi) = R(p) + \varepsilon S(p, \phi) + O(\varepsilon^2). \quad (22)$$

We will show that, in order to compute the SSM for second-order systems, it suffices to solve the invariance equation for the displacement parametrization w_ε only. Subsequently, the velocity parametrization $\dot{w}_\varepsilon$ can be analytically reconstructed by differentiating w_ε with respect to time.

B. Autonomous SSM ($\varepsilon = 0$)

In order to compute autonomous SSMs, the *autonomous invariance equation*

$$B(DW(p))R(p) = A W(p) + F(W(p)) \quad (23)$$

must be solved. This equation is obtained by substituting the expansions (21) and (22) into the invariance equation (17) and collecting terms at $\mathscr{O}(\varepsilon^0)$. As we have noted, expansions of the SSM parametrization and the reduced dynamics will be written using multi-indices. A multi-index m is a vector $m \in \mathbb{N}^M$ for which addition, subtraction, and other operations are defined elementwise. With the help of multi-indices, multivariate monomials can be written as $p^m = p_1^{m_1} \cdots p_M^{m_M}$.

The autonomous parametrizations of the SSM are expanded using these multi-indices

$$w(p) = \sum_{m \in \mathbb{N}^M} w_m p^m, \quad (24)$$

$$\dot{w}(p) = \sum_{m \in \mathbb{N}^M} \dot{w}_m p^m, \quad (25)$$

where $w_m, \dot{w}_m \in \mathbb{C}^n$. As we elaborate in Appendix A 1 b, when compared to tensor-based approaches,[34,53,61] this notation results in a drastic reduction in the number of systems of equations that need to be solved, depending on the SSM dimension and the order of approximation. For instance, in the case of two-dimensional SSMs, we observe an exponentially lower number of equations for multi-index notation relative to the tensor notation as the order of approximation increases.

The autonomous reduced vector field $R(p)$ is also expanded using multi-index notation as

$$R(p) = \sum_{m \in \mathbb{N}^M} R_m p^m, \quad R_m = \begin{bmatrix} R_m^1 \\ \vdots \\ R_m^M \end{bmatrix}. \quad (26)$$

Substituting the expansions (24)–(26) into the autonomous invariance equation (23) results in a linear system of equations that can be solved recursively at each order for the unknown coefficients W_m and R_m. These equations are decoupled for distinct multi-indices at each order. Furthermore, the splitting (24) of the parametrization yields a single n-dimensional system of linear equations that can be solved for the displacement coefficients w_m according to the following statement.

Lemma 1. *The cohomological equation associated with the autonomous invariance equation (23) for a multi-index m can be written as*

$$\underbrace{\left(K + \Lambda_m C + \Lambda_m^2 M \right)}_{:=L_m} w_m = D_m R_m + C_m, \quad (27)$$

where $C_m \in \mathbb{C}^n$, $D_m \in \mathbb{C}^{n \times M}$ are defined in Appendix A 2, and $\Lambda_m = \Lambda \cdot m$ with $\Lambda = (\lambda_1, \ldots, \overline{\lambda}_{M/2})$.

Proof. See Appendix A 2. □

In system (27), the matrix D_m is computed solely based on the eigenvalues and eigenvectors associated with the master subspace, whereas C_m contains contributions from the lower-order terms in the expansion of the SSM and its reduced dynamics. Based on Lemma 1, the system (27) can be solved recursively up to any arbitrary order for the autonomous coefficients w_m, R_m of the SSM parametrization and the reduced dynamics. At any order m, we have $z_m = \binom{m+M-1}{M-1}$ distinct multi-indices in the expansions (24) and (26). Thus, at each order, we need to solve z_m systems of n-dimensional linear equations. Indeed, for real dynamical systems, symmetries allow for further reduction in the number of equations.

Remark 1. In case of near-resonances of the form

$$\lambda_i \approx \Lambda_m, \tag{28}$$

the coefficient matrix L_m will be nearly singular (see, e.g., Ref. 34). If the resonance condition (28) is fulfilled for any eigenvalue $\lambda_i \in \text{Spec}(\mathscr{E})$ then a nonzero choice for R_m is necessary to solve the linear system (27), where different choices lead to different styles of parametrization.[34,48]

To understand the resonance condition (28), consider a two-dimensional SSM tangent to a modal subspace spanned by lightly damped (complex–conjugate) modes with associated eigenvalues λ and $\bar{\lambda}$ satisfying

$$\lambda \approx l\lambda + (l-1)\bar{\lambda}, \tag{29}$$

for all small enough $l \in \mathbb{N}^+$. This relationship holds for the pair $(\lambda, \bar{\lambda})$ if its real part is small, i.e., the underlying physical system is lightly damped. In this case, for any multi-index of the form $m = [l, l-1]$, the coefficient matrix L_m in system (27) turns out to be nearly singular.

Finally, once we have computed the coefficients w_m for the displacement parametrization $w(p)$, the coefficients for the velocity parametrization can be directly obtained using the following statement.

Lemma 2. *The coefficients of the velocity parametrization corresponding to a multi-index m can be obtained directly from the displacement parametrization as*

$$\dot{w}_m = [Dw(p)R(p)]_m. \tag{30}$$

Proof. See Appendix A 2. □

C. Non-autonomous SSM ($\varepsilon > 0$)

In the non-autonomous setting, inserting the expansions (21) and (22) into the invariance equation (17), and collecting terms of $\mathscr{O}(\varepsilon)$ leads to the *non-autonomous invariance equation*

$$B\Big((DW(p))S(p,\phi) + [\partial_p X(p,\phi)]R(p) + [\partial_\phi X(p,\phi)]\Omega\Big)$$
$$= AX(p,\phi) + \big[DF(W(p))\big]X(p,\phi) + G(W(p,\phi),\phi), \tag{31}$$

which needs to be solved for the non-autonomous terms X and S in the parametrizations for the SSM and its reduced dynamics. As in the autonomous case, we now expand the nonlinear functions in Taylor series using multi-indices. The coefficients of these series, however, depend quasiperiodically on time. Hence, we

further expand these coefficients in temporal Fourier series to obtain

$$x(p,\phi) = \sum_{m \in \mathbb{N}^M} \sum_{\kappa \in \mathbb{Z}^K} x_{m,\kappa} e^{i\langle \kappa, \phi \rangle} p^m, \tag{32}$$

$$\dot{x}(p,\phi) = \sum_{m \in \mathbb{N}^M} \sum_{\kappa \in \mathbb{Z}^K} \dot{x}_{m,\kappa} e^{i\langle \kappa, \phi \rangle} p^m. \tag{33}$$

The reduced dynamics are similarly expanded in a Taylor–Fourier Series as

$$S(p,\phi) = \sum_{m \in \mathbb{N}^M} \sum_{\kappa \in \mathbb{Z}^K} S_{m,\kappa} e^{i\langle \kappa, \phi \rangle} p^m, \quad S_{m,\kappa} = \begin{bmatrix} S_{m,\kappa}^1 \\ \vdots \\ S_{m,\kappa}^M \end{bmatrix}. \tag{34}$$

The procedure of determining these coefficients recursively is similar to that of the autonomous case. The contributions to distinct harmonics and to different multi-indices can be considered independently as the corresponding equations decouple. For second-order systems, the computation of these coefficients can again be carried out by first obtaining the displacement parametrization $x(p,\phi)$ via a cohomological equation of dimension n, followed by computing the velocity parametrization $\dot{x}(p,\phi)$ directly from the time derivative of the displacement terms, as we detail below.

Lemma 3. *The cohomological equation associated with the non-autonomous invariance equation (31) for the multi-index m and the harmonic κ is given by*

$$\underbrace{\left(K + \Lambda_{m,\kappa} C + \Lambda_{m,\kappa}^2 M\right)}_{L_{m,\kappa}} x_{m,\kappa} = D_{m,\kappa} S_{m,\kappa} + C_{m,\kappa}, \tag{35}$$

$C_{m,\kappa} \in \mathbb{C}^n$, $D_{m,\kappa} \in \mathbb{C}^{n \times M}$ *are defined in Appendix A 2, and* $\Lambda_{m,\kappa} := \Lambda \cdot m + i\Omega \cdot \kappa$.

Proof. See Appendix A 2. □

In system (35), the matrix $D_{m,\kappa}$ depends on the eigenvalues and eigenvectors of the master subspace as well as on the forcing frequency Ω. The vector $C_{m,\kappa}$ contains contributions from lower-order terms in the parametrization of the SSM and its reduced dynamics. The system (35) contains decoupled equations for each pair of multi-indices and harmonics (m, κ). Thus, for z_m distinct multi-indices and z_K distinct harmonics, we must solve $z_m z_K$ systems of n-dimensional linear equations.

Remark 2. In case of near-resonances of the form

$$\lambda_i \approx \Lambda \cdot m + i\Omega \cdot \kappa, \tag{36}$$

the coefficient matrix $L_{m,\kappa}$ will be nearly singular (see, e.g., Refs. 34 and 60). If the resonance condition (28) is fulfilled for any eigenvalue $\lambda_i \in \text{Spec}(\mathscr{E})$, then a nonzero choice for $S_{m,\kappa}$ is necessary to solve the linear system (27), where different choices lead to different styles of parametrization.[34,48]

As an example of the resonance condition (36), consider a two-dimensional periodic SSM. At the leading order, the resonance condition then reduces to $\lambda \approx i\Omega$, which is a simple resonance created by the external periodic excitation. Higher-order terms lead to more complicated resonances, which are able to capture the effects of parametric resonance. For instance, the principal parametric resonance of the form $\Omega \approx 2\text{Im}(\lambda)$ results from the near-resonance

relationship

$$\lambda \approx \overline{\lambda} + i\Omega \qquad (37)$$

in terms of Eq. (36) (see also Ref. 61). Finally, once we have computed the coefficients $\boldsymbol{x}_{m,\kappa}$ for the displacement parametrization $\boldsymbol{x}(\boldsymbol{p}, \boldsymbol{\phi})$, the coefficients for the nonautonomous velocity parametrization can be obtained directly using the following statement (cf. Lemma 2).

Lemma 4. *The coefficients of the nonautonomous velocity parametrization $\dot{\boldsymbol{x}}_{m,\kappa}$ for a multi-index $\boldsymbol{m}$ and harmonic $\boldsymbol{\kappa}$ can be computed directly from the displacement parametrization as*

$$\dot{\boldsymbol{x}}_{m,\kappa} = [D\boldsymbol{w}(\boldsymbol{p}) \cdot \boldsymbol{S} + \partial_p \boldsymbol{x} \cdot \boldsymbol{R} + \partial_\phi \boldsymbol{x} \cdot \boldsymbol{\Omega}]_{m,\kappa}. \qquad (38)$$

Proof. See Appendix A 2. □

Remark 3. For mechanical systems with proportional damping and geometric nonlinearities up to cubic-order, prior works[53,61] exploited the second-order nature of the equations of motion to reduce the number of cohomological equations by a factor of half relative to their first-order counterpart. Indeed, such a reduction in the number of equations arises from the underlying structure (19) of the phase-space variables in any second-order system. Hence, Lemmas 1–4 allow explicit extension of these computational advantages to general second-order systems with nonlinearities of arbitrary polynomial order, including nonlinear damping.

We note that once the autonomous part of the SSM is computed up to a chosen order of approximation o, the order of approximation o_1 of the non-autonomous part of the SSM may be chosen independent of o as long as $o_1 < o$. Consequently, given an order of approximation o for the autonomous part, the maximal accuracy for the non-autonomous computation will be obtained when $o_1 = o - 1$. In specific cases, choosing $o_1 < o - 1$ may also provide satisfactory accuracy at lower computational costs (see, e.g., Ref. 61 for the effect of choices of o_1 in systems with direct external excitation).

V. STABILITY DIAGRAMS AND SSM

A. Mathematical foundation

In this section, we consider mechanical systems subject to periodic parametric excitation, which means that $\boldsymbol{f}^{ext} = \boldsymbol{0}$ in Eq. (2). For such systems, $\boldsymbol{z} = \boldsymbol{0}$ remains a fixed point for system (3) even for $\varepsilon > 0$. This fixed point may, however, be destabilized by resonances between the eigenfrequencies of the linear system and the parametric excitation frequency.

In order to study the stability of this fixed point for $\varepsilon > 0$, the dynamical system (3) can be extended to an autonomous system of variables $(\boldsymbol{z}, \tau) \in \mathbb{R}^N \times S^1$ such that the trivial fixed point can be interpreted as the zero-amplitude periodic orbit $(\boldsymbol{z}, \tau) = (\boldsymbol{0}, t \bmod 2\pi)$.[1] Changes in the stability of this periodic orbit result in bifurcations with respect to parameters. Numerical continuation of periodic orbits is needed to locate an initial bifurcation with respect to the forcing frequency or the forcing amplitude, as shown in Fig. 1. Once this bifurcation is detected, it must be continued in the parameter space to obtain a family of such bifurcations that define the stability boundary. Tools such as the po toolbox of the continuation package COCO[28] employed in this work can detect and continue families of such bifurcations using Floquet theory (we refer
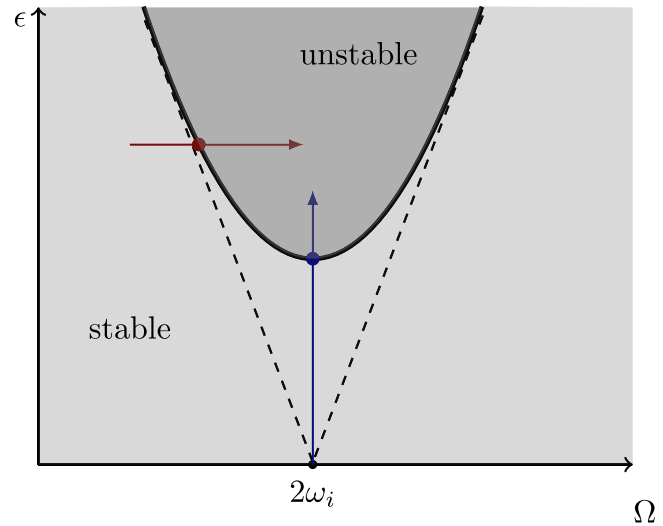
FIG. 1. Sketch of a stability diagram at the principal resonance. The thin dashed line corresponds to the boundary of stable and unstable regions in the conservative limit. When damping is added, the tongue starts to lift up, bounded by the thick black line. The numerical continuation in the variables ε (blue arrow) and Ω (red arrow), respectively, leads to the detection of a bifurcation indicated by the blue and red dots. Choosing these bifurcations as a starting point, the family of bifurcations on the boundary can then be found via further continuation.

to Dankowicz and Schilder[28] for a detailed account). We employ SSM computation in order to efficiently obtain the *resonance tongue* of the principal resonance, which marks the stability boundary in Fig. 1. The SSM is constructed over the spectral subspace corresponding to the resonant eigenfrequency ω_i. Consequently, the M-dimensional ROM

$$\dot{\boldsymbol{p}} = \boldsymbol{R}_\varepsilon(\boldsymbol{p}, \Omega t) \qquad (39)$$

$$= \sum_{\boldsymbol{m} \in \mathbb{N}^M} \boldsymbol{R}_m \boldsymbol{p}^m + \varepsilon \sum_{\substack{\boldsymbol{m} \in \mathbb{N}^M \\ m \geq 1}} \sum_{\kappa \in \mathbb{Z}} \boldsymbol{S}_{m,\kappa} e^{i\kappa\Omega t} \boldsymbol{p}^m \qquad (40)$$

needs to be analyzed for bifurcations. Details on the corresponding continuation problems are recounted in Appendix C. As the forcing frequency changes, the ROM has to be updated, which highlights the need for a fast computational algorithm to calculate the SSM. The reduced dynamics are of low dimension, so continuation is a suitable method, as it is fast on small systems and provides key insights into the bifurcation behavior. The proposed approach, thus, combines the advantages of reduced-order modeling and numerical continuation.

B. Computational complexity

Here, we briefly discuss the computational complexity of approximating the periodic response via two-dimensional SSMs and compare it to that of the collocation method applied to the full system.

1. Master subspace: This step involves the solution of the eigenvalue problem (7) to obtain the two eigenvalues and eigenvectors associated with the two-dimensional master subspace.

2. Autonomous SSM: For computing the order-i approximation to an autonomous, two-dimensional SSM, the coefficient vectors, $w_m \in \mathbb{R}^n$, for $(i+1)$ monomials, $m \in \mathbb{N}_0^2$, need to be obtained. Thus, to compute the autonomous SSM and its reduced dynamics up to order Γ, we need to solve the n-dimensional linear system (27) a total of

$$\Sigma_\Gamma := \sum_{i=2}^{\Gamma}(i+1) = \frac{1}{2}(\Gamma+1)(\Gamma+2) - 3 \qquad (41)$$

times. These computations are independent of the forcing and can be parallelized over each monomial m in a given order.

3. Non-autonomous SSM: At each forcing harmonic, $\kappa \in \mathbb{Z}$, we have $\sum_{i=0}^{\Gamma-1} i+1$ monomials that determine the non-autonomous SSM coefficients $w_{m,\kappa} \in \mathbb{R}^n$ at order Γ. Thus, for a system with h harmonics, we need to solve the n-dimensional linear system (35), a total of

$$\Sigma_{\Gamma,h} := h\sum_{i=0}^{\Gamma-1}(i+1) = \frac{h}{2}\Gamma(\Gamma+1) \qquad (42)$$

times. These computations need to be performed for each forcing frequency but can be parallelized over each harmonic κ and monomial m in a given order.

4. Reduced periodic response computation via collocation-based numerical continuation: Once the SSM and its two-dimensional reduced dynamics are computed, we approximate a periodic solution of the reduced system via the collocation method. Approximating the nonlinear periodic response via c collocation points in a d-dimensional dynamical system requires the solution of cd-dimensional system of coupled nonlinear algebraic equations.[28,65] Typically, this is achieved iteratively by solving a cd-dimensional linearized system i times (iterations) until a solution is found via an iterative solver, such as the Newton–Raphson method. This periodic solution is then numerically continued in the parameter space to obtain the FRC or stability diagrams. Note that we have $d = 2$ for a two-dimensional SSM-based ROM. We have $d = 2n$ when the same method is applied to the full system but steps 1–3 are not required in that case.

For the direct solution of an n-dimensional linear system and the associated eigenvalue problem in step 1, we conservatively assume a cubic computational complexity $\mathcal{O}(n^3)$.[63] We summarize the above steps and their associated computational complexity to obtain stability diagrams/FRCs via the SSM-based ROM and via full-system collocation in Table VI (see Appendix C 3).

As the system size n increases, the main computational bottleneck for numerical solutions will be the assembly and inversion of the system matrix. We note from Table VI that the maximal dimension of the system matrix in SSM-based ROM computations is n, but it is $2nc$ for full-system collocation. For sufficient accuracy, one often employs a number of collocation points in the range of $c \in [10, 100]$, which increases the dimension of the system matrix

by several orders of magnitude. This results in significantly higher requirements of computational resources for full-system collocation relative to SSM-based ROMs, as n becomes large.

Apart from the distinctions in computational complexity, the local nature of SSM-based computations is worth emphasizing, since the Taylor–Fourier approximations of the SSMs generally have only a limited radius of convergence. Numerical continuation of the full system, on the other hand, seeks globally accurate approximations by stitching together local solution patches. Consequently, isolated solution branches (or isolas) would generally be missed by numerical continuation in the absence of an initial solution on the isolated branch, as we show in the examples of Sec. VI.

C. Examples

We now compare the SSM-based ROM predictions to full-system simulations in terms of accuracy and computational performance. To this end, we implemented the procedure for computing nonautonomous SSMs and the related numerical examples in the MATLAB-based package SSMTool 2.4.[62] The numerical continuation of the nonlinear response of the full system as well as of the SSM-based ROM are performed using the MATLAB-based numerical continuation package COCO.[28] When reporting the computation times for SSM-based ROMs, we also include any time spent on ROM construction, such as computation of the non-autonomous SSMs and their reduced dynamics for different forcing frequencies, mapping the reduced results onto the full phase space. All computations in this section are performed using MATLAB 2023a on a Apple M2-CPU @3.49 GHz with 24 GB of RAM. We remark that we report the computational times only for completeness and not to establish computational benchmarks. The speed and convergence of numerical continuation is dependent on several numerical parameters, and the available implementations in COCO[28] may lead to sub-optimal performance. Furthermore, the dimension of the full system in the examples we consider may not be high enough to truly appreciate the computational savings associated with SSM-based ROMs.

1. Mathieu equation

The most frequently discussed system in the parametric excitation literature is the Mathieu equation

$$m\ddot{y} + c\dot{y} + \omega_0^2(1 + \varepsilon \cos \Omega t)y = 0, \quad 0 \ll \varepsilon \ll 1, \qquad (43)$$

whose stability is well understood. Various studies have appeared for the damped and undamped cases,[14] some with additional nonlinearities to system[6] and others in higher dimensions.[37] Here, we extend the system (43) to a set of damped oscillators coupled via springs with parametrically varying stiffness. Adding stiffness nonlinearities then results in the mechanical system displayed in Fig. 2. The resulting generalized Mathieu equation is given by

$$M\ddot{y} + C\dot{y} + \left(K + \varepsilon Q \cos(\Omega t)\right)y + f(y) = 0. \qquad (44)$$
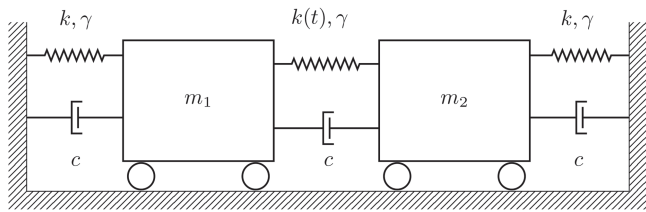
FIG. 2. Schematic model of two oscillators described by two coupled Mathieu equations. The coupling springs have time-varying stiffness coefficients $k(t) = k(1 + \varepsilon \cos(\Omega t))$. The induced parametric excitation may destabilize the trivial fixed point if chosen in subharmonic resonance with an eigenfrequency of the linearized dynamical system.

In the case considered here, these matrices and the nonlinearity are explicitly given as

$$M = \begin{bmatrix} m_1 & 0 \\ 0 & m_2 \end{bmatrix}, C = \begin{bmatrix} 2c & -c \\ -c & 2c \end{bmatrix}, K = \begin{bmatrix} 2k & -k \\ -k & 2k \end{bmatrix}, \tag{45}$$

$$Q = \begin{bmatrix} k & -k \\ -k & k \end{bmatrix}, f(y_1, y_2) = \kappa \begin{bmatrix} -y_1^3 - (y_1 - y_2)^3 \\ -y_2^3 + (y_1 - y_2)^3 \end{bmatrix}. \tag{46}$$

We choose non-dimensional parameters $m_i = 1, k = 1, c = 0.05$, and $\kappa = 0.1$, for which we obtain the eigenvalues of the $\varepsilon = 0$ system in the form $\lambda_1, \overline{\lambda_1} \approx -0.0250 \pm 0.9997i$ and $\lambda_2, \overline{\lambda_2} \approx -0.0500 \pm 1.7304i$. Both these modes exhibit parametric instabilities at resonance. For each mode, this instability can be analyzed by computing the corresponding SSM and its reduced dynamics. We choose to analyze the nonlinear response under the principal parametric resonance $\Omega \approx 2\omega_2$ by constructing the non-autonomous SSM corresponding to the spectral subspace $\mathscr{E} = \text{span}(v_2, \overline{v_2})$. Using numerical continuation in the reduced dynamics, we will detect the corresponding resonance tongue.

First, we choose an initial parameter set $(\varepsilon_i, \Omega_i)$, then either of the two parameters is released, and the trivial $2\pi/\Omega_i$-periodic response is continued in search of period-doubling bifurcations. The detected bifurcation point is then continued in the parameter space, yielding the stability diagram in Fig. 3(a). The entire procedure is automated, constantly updating the coefficients of the nonautonomous reduced dynamics when the excitation frequency gets changed.

To obtain a more complete picture of how these regions of stability influence the system's dynamics, we consider the non-trivial forced response of system (44), which emanates from the instability. The orbits with period $T = \frac{4\pi}{\Omega} \approx \frac{2\pi}{\omega_2}$ bifurcate out of the trivial response at the stability boundary. The amplitude of these response curves increases smoothly with increasing excitation amplitude ε. The reduced dynamics on the SSM serves as a ROM to explore periodic orbit families via numerical continuation. The resulting forced response and the stability diagram are shown in Fig. 3. The resonance tongue and the forced response are accurately reproduced using the ROM, as we verify using the po-toolbox of COCO on the full dynamical system. The parameters used for continuation of the full and reduced models are noted in Appendix C.
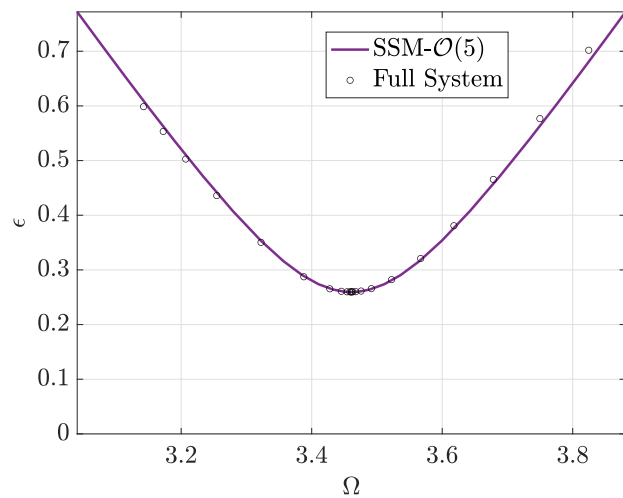
(a)
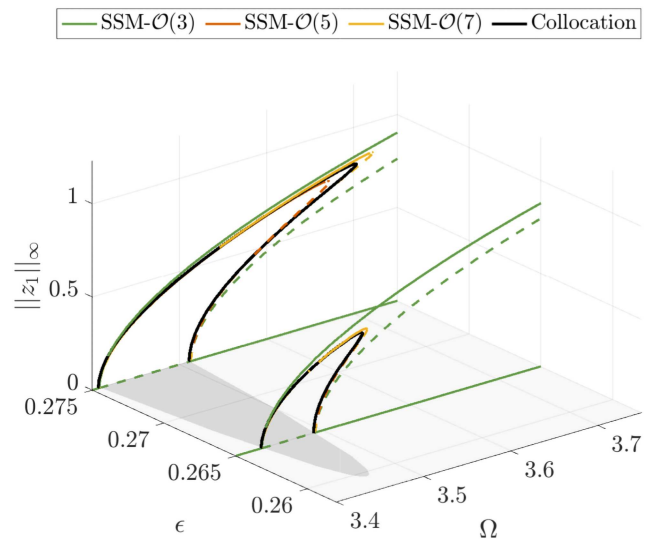
(b)

FIG. 3. Stability diagram and forced response of the two coupled Mathieu oscillators shown in Fig. 2. (a) Stability diagram of the second mode obtained using an SSM-based ROM, which locally approximates the resonance tongue in a region around the principal resonance where $\Omega \approx 2\omega_2$. (b) The $||z_1||_\infty = 0$ plane corresponds to the trivial response of the full system. On this plane, the resonance tongue is displayed in gray shades. From its boundary, orbits with period $4\pi/\Omega$ emerge that show hardening behavior due to the nonlinearity.

The computation time for the stability diagram using the full system was 5 s. The same computation using the ROM, including the continual update of the SSM parametrization, takes 33 s. Similarly, for the FRCs displayed in Fig. 3(b), the full-system analysis took 22 s, while using the $\mathscr{O}(7)$ ROM amounted to 3 min and 38 s.

TABLE I. Physical parameters used for the model of the Bernoulli beam.

Symbol	Meaning	Value
L	Length of beam	2700 (mm)
h	Thickness of beam	10 (mm)
b	Width of beam	10 (mm)
E	Young's modulus	45×10^6 (kPa)
I	Area moment of inertia	833.3 (mm^4)
α	Structural damping parameter	1.25×10^{-4} (s^{-1})
β	Structural damping parameter	2.5×10^{-4} (s)
κ	Cubic stiffness coefficient	50 (mN/mm^3)
γ	Cubic damping coefficient	-0.01 (mNs/mm^3)

Therefore, because the full dynamical system is low-dimensional, the advantage of using a ROM is outweighed by the computational cost of constructing the reduced dynamics and the time-dependent SSM for each forcing frequency.

2. Bernoulli beam

We now consider the nonlinear Bernoulli beam shown in Fig. 4(a) and treated in Ref. 54. It is clamped on one side and subjected to a cubic spring, a cubic damper, and parametric excitation at its free end and moves in the $x - z$ plane. A similar example has been experimentally studied by Chen and Yeh,[66] who implemented parametric excitation through a pair of coils fixed to the beam. Nearby magnets mounted on a support were then used to exert a force on these coils when a current is applied.

We discretize the beam, resulting in n degrees of freedom. Damping is assumed to be proportional and of the form $C = \sigma(\alpha M + \beta K)$. Here, the cubic nonlinearity $f(y, \dot{y})$ includes the nonlinear damping coefficient γ and the nonlinear stiffness κ. The parameters and beam properties are set according to Table I. Compared to the original parameter value $\kappa = 6$ mN/mm^3 used in Ref. 54, we consider a stronger cubic nonlinearity in the spring with $\kappa = 50$ mN/mm^3. Furthermore, we add parametric excitation to the system given by

$$f_{\text{param}}(\Omega t, y) = \varepsilon \cos \Omega t Q y, \qquad (47)$$

where $Q \in \mathbb{R}^{n \times n}$ is a Boolean matrix that performs projection onto the $z-$DOF at the tip of the beam. This system is driven in the regime of parametric resonance by targeting the principal resonance of the mode associated with the leading pair of eigenvalues

$$\lambda_1, \overline{\lambda_1} \approx -0.1238 \pm 6.9995i. \qquad (48)$$

The principal resonance is, thus, obtained for forcing frequency values $\Omega \approx 13.999$ rad/s. We use the reduced dynamics on the corresponding SSM to construct the stability diagram of the principal resonance of the selected mode. The resulting resonance tongue is shown in Fig. 5(a) for various values of the damping coefficient σ. The forced response based on SSM computations for a set of parametric excitation amplitudes is shown in Fig. 5(b). Due to the strongly nonlinear nature of this example, we observe nonlinear phenomena at lower response amplitudes compared to the thickness of the beam (see also Ref. 54, where the merger of an isola with

(a)

(b)
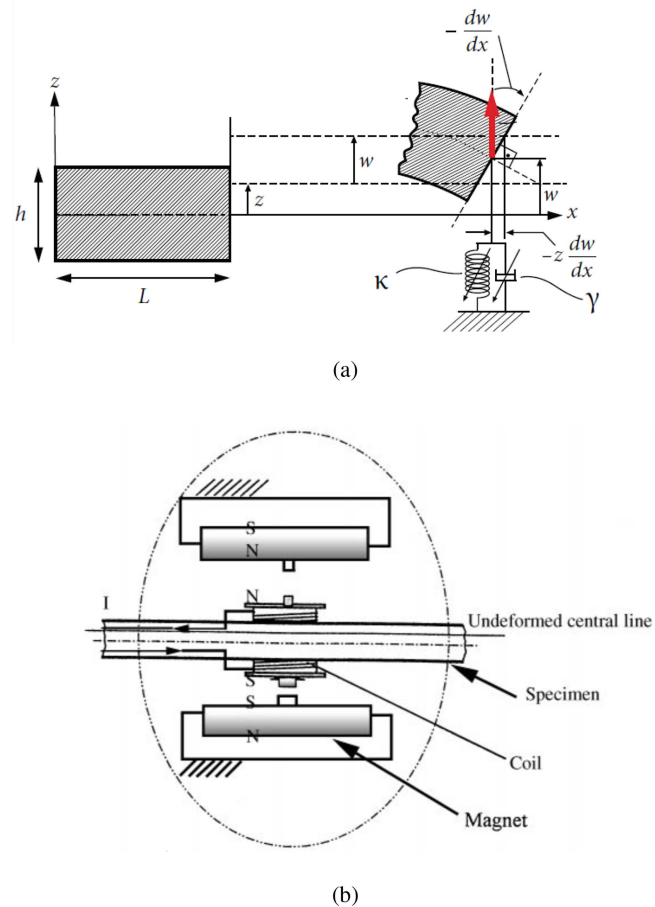
FIG. 4. (a) Model of a linear Bernoulli beam of length L and thickness h as treated by Ponsioen et al.[54] The beam is aligned with the x axis and parametrically excited on the free end, as indicated by the red arrow. A nonlinear (cubic) damper and a cubic spring are attached to the free end of the beam. (b) Schematic depiction of a possible experimental setup for parametrically exciting the beam, reproduced with permission from Chen and Yeh, J. Sound Vib. **240**, 747–764 (2001).[66] Copyright 2001, Elsevier. Two coils are used as tunable magnets via the induced current I. Depending on its magnitude and direction, the effective attraction and repulsion between the beam and the adjacent magnets can be controlled. This results in a time varying stiffness.

the main branch of the response is observed near the displacement amplitude of 0.05 mm).

We compare the SSM-reduced results with the corresponding full system's results computed using the collocation method implemented in COCO,[28] for which the relevant simulation parameters can be found in Appendix C. In Fig. 5(b), we observe that for smaller values of the excitation amplitude ε, the SSM-reduced results converge to the full-system solution as the order of SSM approximation increases from 3 to 7. For higher excitation amplitudes, however, we observe that the SSM-reduced results start deviating from the full system's response. Indeed, this observation agrees with SSM
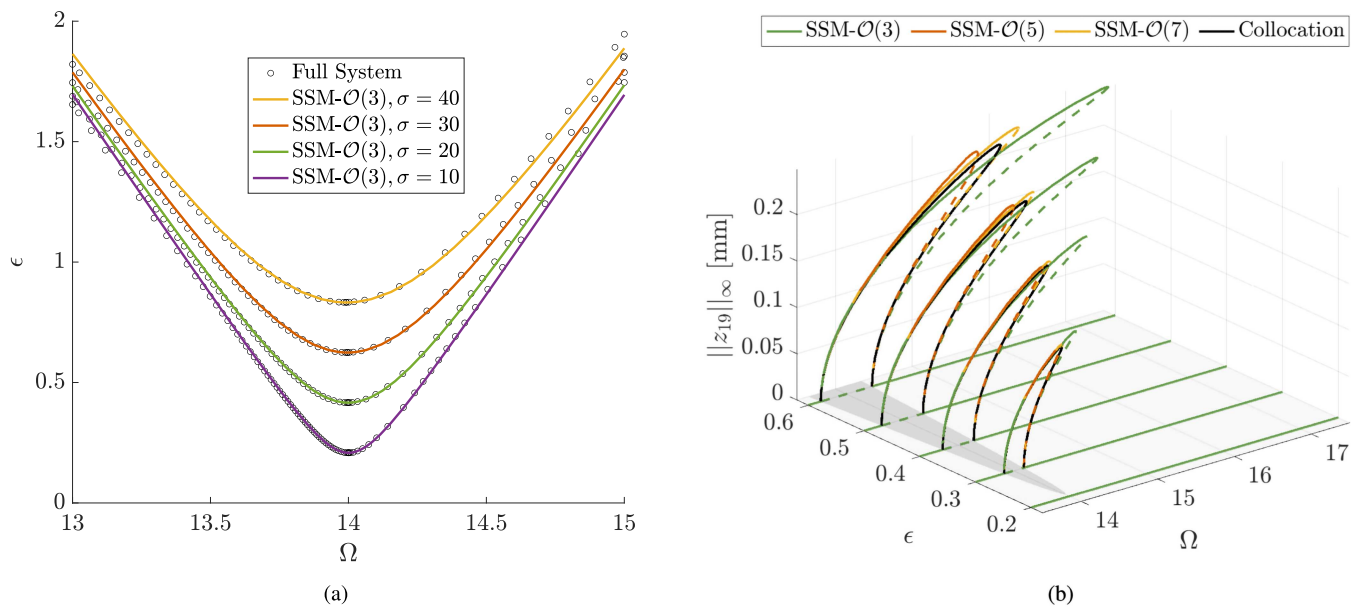
FIG. 5. (a) Stability diagram for the principal resonance of the first mode of the Bernoulli beam for 10 elements with $n = 20$ degrees of freedom. The solid line denotes the border of the resonance tongues as obtained using the dynamics of the full system and has been obtained via the collocation method. The reduced dynamics provided by a cubic truncation of the SSM accurately locates the position and shape of the tongue for different values of the damping parameter σ. (b) Forced response along the transverse DOF, z_{19}, located at the tip of the beam. Nontrivial periodic response branches of period $T = 4\pi/\Omega$ emanating from the stability boundary via period-doubling bifurcations. The amplitude of the response curve increases with growing parametric excitation amplitude ε. The results for different orders of approximation of the manifold and reduced dynamics are plotted to visualize the convergence of the reduced response to the full solution.

theory,[49] which is applicable for limited forcing amplitudes (see also Ref. [35]).

The computation times for the stability diagram and forced responses are reported in Tables II and III, which show that the computational savings arising from the use of SSM-based ROM in this higher-dimensional example are significant, unlike in our first example.

3. Prismatic beam

Next, we analyze the dynamics of a hinged-clamped prismatic beam. Extending the initial treatment of external excitation by Nayfeh *et al.*,[67] Li *et al.*[35] have recently applied SSM theory to the case of a 1:3 internal resonance between the first two bending modes of this beam model. Their implementation serves as the basis of this example but we choose the nondimensionalized length in terms of

the characteristic length here as $l = 1.7$ to avoid internal resonances. Introducing nondimensional parameters and coordinates, Nayfeh *et al.*[67] derive nonlinear partial equations for the transverse displacement $w(y, t)$ of the beam. Under axial loading at the hinged tip, these equations must be modified to[68]

$$\frac{\partial^4 w}{\partial y^4} + \frac{\partial^2 w}{\partial t^2} = \delta \left(H \frac{\partial^2 w}{\partial y^2} - p_a(t) \frac{\partial^2 w}{\partial y^2} - 2c \frac{\partial w}{\partial t} \right), \quad (49)$$

where $p_a(t)$ describes the axial loading, δ is the slenderness ratio of the beam, H accounts for the axial stretching forces that depend on w [see Eq. (D5) in Appendix D for the explicit expression], and c is the distributed damping parameter. We refer to Appendix D for the mathematical expressions of various dimensionless parameters in Eq. (49). The axial excitation effectively leads to a parametric excitation on the transverse displacements of the beam, as is evident in Eq. (49). The beam is clamped at $y = l$ and hinged at $y = 0$, resulting

TABLE II. Computation time for the stability diagrams in Fig. 5(a) with $n = 20$ DOFs in the format hh:mm:ss.

Damping (σ)	SSM $\mathcal{O}(3)$	Full system
10	00:00:15	00:02:13
20	00:00:10	00:01:52
30	00:00:08	00:01:36
40	00:00:07	00:01:27

TABLE III. Computation time for the sweep of FRCs in Fig. 5(b) with $n = 20$ DOFs in format hh:mm:ss. The damping parameter is chosen as $\sigma = 10$.

Algorithm	Computation time
Full-system collocation	00:52:30
SSM $\mathcal{O}(3)$	00:01:16
SSM $\mathcal{O}(5)$	00:02:28
SSM $\mathcal{O}(7)$	00:05:50

(a)
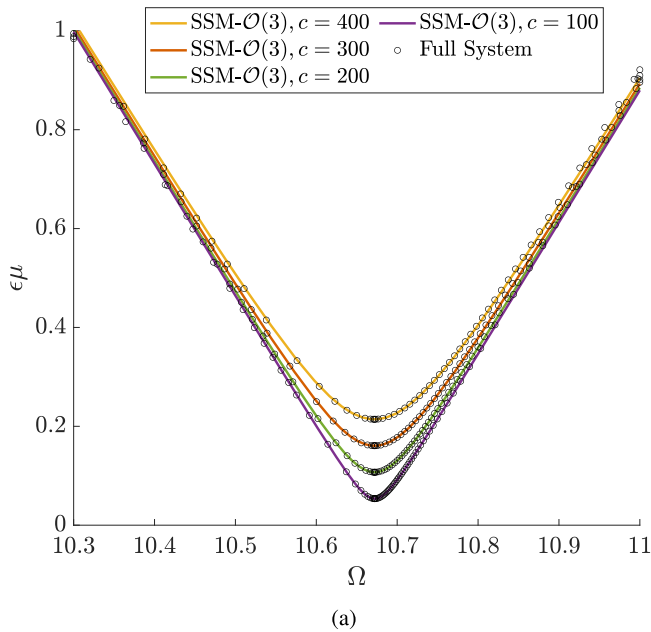
FIG. 6. Stability diagram for the principal resonance of the first mode of the prismatic beam for a truncation with $n = 10$ modal coordinates. The full-system response has been obtained with the use of collocation. The reduced model of these full dynamics given by the dynamics on the SSM can accurately predict the stability behavior of the full system.

in the boundary conditions

$$w(0) = w(l) = 0, \quad w'(l) = 0, \quad w''(0) = 0. \quad (50)$$

After writing the displacement $w(y, t)$ as a modal expansion, we obtain a system of second-order ODEs for the evolution of the modal amplitudes $z_j(t)$,

$$\ddot{z}_j + 2\delta c \dot{z}_j + \omega_j^2 z_j = \sum_{i,k,s} \delta\alpha_{jiks} z_i z_k z_s + \delta \sum_i p_a(t) z_i a_{ji}, \quad (51)$$

with $i, j, k, s \in \{1, \ldots, n\}$. A detailed derivation of these equations using Galerkin projection along with the definition of the coefficients α_{jiks} and a_{ji} is given in Appendix D. We take the axial forcing to be harmonic and of the form

$$p_a(t) = \mu \cos(\Omega t). \quad (52)$$

Furthermore, we set $\delta = 1 \times 10^{-4}$. The modal expansion is truncated at n modes, which gives rise to a phase space dimensionality of $N = 2n$.

We wish to analyze the stability of the beam when axially excited at the principal resonance of its fundamental frequency. We construct the SSM over the first pair of modes with eigenvalues

$$\lambda_1, \overline{\lambda_1} \approx -0.0200 \pm 5.3361i. \quad (53)$$

The instability of the trivial fixed point induced by the parametric resonance occurs near the excitation frequency values $\Omega \approx 10.6672$[rad/s]. Figure 6 shows the corresponding stability diagram and Fig. 7 shows the steady-state response computed using the SSM-based ROM. The full system's stability is again verified using

(a)

(b)
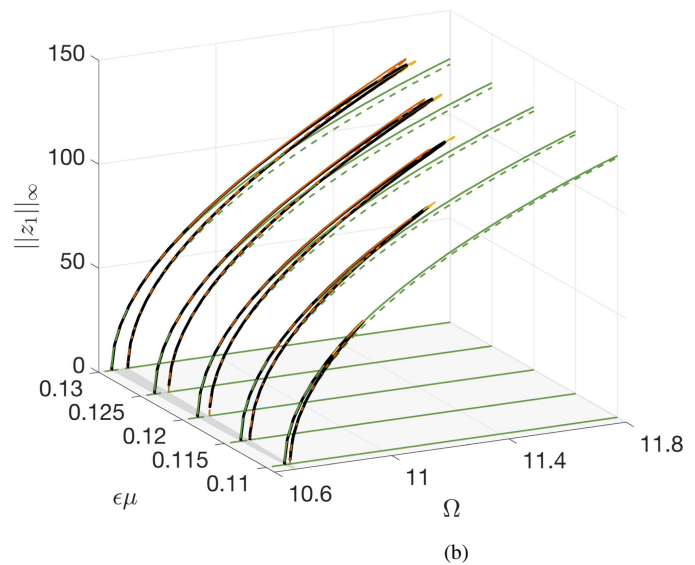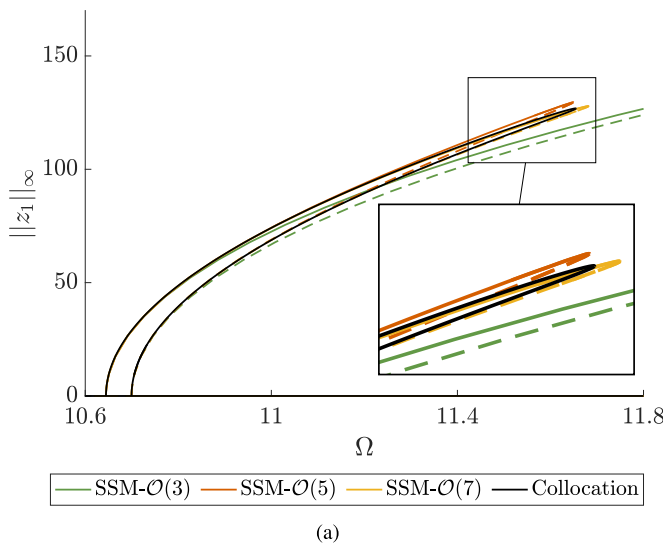
FIG. 7. Forced response of the prismatic beam along the parametrically excited modal coordinate z_1 [see Eq. (51)]. (a) Nontrivial periodic response branch of period $T = 4\pi/\Omega$ emerging out of the stability boundary (see Fig. 6) via a period-doubling bifurcation for $\varepsilon\mu = 0.13$, $c = 200$, and $n = 10$. (b) Forced response for various excitation amplitudes.

TABLE IV. Computation time for the stability diagrams of the prismatic beam example with $n = 10$ DOFs in Fig. 6, given in hh:mm:ss.

Damping (c)	SSM $\mathcal{O}(3)$	Full system
100	00:00:17	00:00:42
200	00:00:10	00:00:36
300	00:00:09	00:00:34
400	00:00:08	00:00:32

the po-toolbox of COCO. The parameters chosen for numerical continuation of the full and reduced system are documented in Appendix C.

Table IV shows the computation times for obtaining the stability diagram in Fig. 6 for different damping parameters and Table V shows the total computation times for obtaining the FRCs in Fig. 7(b) at different excitation amplitudes. Again, the use of an SSM-based ROM brings a significant computational advantage over the full model.

VI. FORCED RESPONSE AND SPECTRAL SUBMANIFOLDS

A. Mathematical foundation

For externally excited systems, SSMs have proven highly effective in capturing the forced response accurately at a low computational cost.[34,52,54,60] Next, we extend these results to obtain FRCs of systems subject to both external and parametric excitation. Our algorithm is completely parallelizable and can be carried out for each forcing frequency independently. We consider periodic external and parametric excitation and assume that their harmonic κ_0 is in 1:1 resonance with the master mode, i.e.,

$$i\kappa_0\Omega \approx \lambda_j, \qquad (54)$$

for some j. We further assume that no (near) internal resonances are present in the spectrum of the dynamical system. The periodic forced response and its stability can then be explicitly computed from the SSM-based ROM according to the following statement.

Lemma 5. *Assume that the near-resonance condition (54) holds for a mechanical system subject to periodic external and parametric excitation. We then obtain the following results for the dynamics on the two-dimensional SSM that serves as the non-autonomous, nonlinear continuation of the jth linear mode:*

TABLE V. Total computation time for the five sweeps of FRCs in Fig. 7(b) for the prismatic beam example with $n = 10$ DOFs, given in hh:mim:ss.

Algorithm	Computation time
Full-system collocation	02:51:52
SSM $\mathcal{O}(3)$	00:02:42
SSM $\mathcal{O}(5)$	00:10:44
SSM $\mathcal{O}(7)$	00:36:14

(i) *Polar dynamics: The reduced dynamics in polar coordinates (ρ, θ) is given by*

$$\begin{bmatrix} \dot{\rho} \\ \rho\dot{\psi} \end{bmatrix} = \boldsymbol{r}(\rho, \psi, \Omega), \qquad (55)$$

$$\dot{\phi} = \Omega, \qquad (56)$$

where

$$\psi = \theta - \kappa_0\phi, \qquad (57)$$

$$\boldsymbol{r}(\rho, \psi, \Omega) = \begin{bmatrix} a(\rho) \\ b(\rho) \end{bmatrix} + \varepsilon\left(\boldsymbol{N}(\psi)\begin{bmatrix} \mathrm{Re}\,(S^1_{\boldsymbol{0},\kappa_0}) \\ \mathrm{Im}\,(S^1_{\boldsymbol{0},\kappa_0}) \end{bmatrix}\right.$$
$$\left. + \sum_{\substack{\boldsymbol{m}\in\mathbb{N}^2 \\ \kappa\in\mathbb{Z}^*}} \rho^{|\boldsymbol{m}|}\boldsymbol{N}((\kappa/\kappa_0)\psi)\begin{bmatrix} \mathrm{Re}\,(S^1_{\boldsymbol{m},\kappa}) \\ \mathrm{Im}\,(S^1_{\boldsymbol{m},\kappa}) \end{bmatrix}\right), \qquad (58)$$

$$a(\rho) = \mathrm{Re}\left(\sum_{\boldsymbol{m}} R^1_{\boldsymbol{m}}\rho^{|\boldsymbol{m}|}\right), \qquad (59)$$

$$b(\rho, \Omega) = \mathrm{Im}\left(\sum_{\boldsymbol{m}} R^1_{\boldsymbol{m}}\rho^{|\boldsymbol{m}|}\right) - \kappa_0\rho\Omega, \qquad (60)$$

$$\boldsymbol{N}(\bullet) := \begin{bmatrix} \cos\,(\bullet) & \sin\,(\bullet) \\ -\sin\,(\bullet) & \cos\,(\bullet) \end{bmatrix}, \qquad (61)$$

and the sum over κ and $\boldsymbol{m}$ includes the harmonics and spatial multi-indices associated with nonzero reduced dynamics coefficients in a normal-form style of parametrization.

(ii) *Forced response curve: The fixed points of the SSM-reduced dynamics lie on the forced response curve that satisfies*

$$\boldsymbol{r}(\rho, \psi, \Omega) = \boldsymbol{0}. \qquad (62)$$

(iii) *Stability of the forced response: For any hyperbolic fixed point (ρ, ψ) of (55), the eigenvalues of the Jacobian,*

$$J = \begin{bmatrix} \partial_\rho a(\rho) & 0 \\ \partial_\rho(b(\rho)/\rho) & 0 \end{bmatrix} + \varepsilon\left(\begin{bmatrix} 0 & d_{\boldsymbol{0},\kappa_0}(\psi) \\ -\frac{d_{\boldsymbol{0},\kappa_0}(\psi)}{\rho^2} & -\frac{c_{\boldsymbol{0},\kappa_0}(\psi)}{\rho} \end{bmatrix}\right.$$
$$\left. + \sum_{\substack{\boldsymbol{m}\in\mathbb{N}^2 \\ \kappa\in\mathbb{Z}^*}} \begin{bmatrix} c_{\boldsymbol{m},\kappa}(\psi)|\boldsymbol{m}|\rho^{|\boldsymbol{m}|-1} & (\kappa/\kappa_0)d_{\boldsymbol{m},\kappa}(\psi)\rho^{|\boldsymbol{m}|} \\ d_{\boldsymbol{m},\kappa}(\psi)(|\boldsymbol{m}|-1)\rho^{|\boldsymbol{m}|-2} & -(\kappa/\kappa_0)c_{\boldsymbol{m},\kappa}(\psi)\rho^{|\boldsymbol{m}|-1} \end{bmatrix}\right), \qquad (63)$$

determine the stability of the fixed point, where

$$c_{\boldsymbol{m},\kappa}(\psi) := \mathrm{Re}\,(S^1_{\boldsymbol{m},\kappa})\cos((\kappa/\kappa_0)\psi)$$
$$+ \mathrm{Im}\,(S^1_{\boldsymbol{m},\kappa})\sin((\kappa/\kappa_0)\psi), \qquad (64)$$

$$d_{\boldsymbol{m},\kappa}(\psi) := -\mathrm{Re}\,(S^1_{\boldsymbol{m},\kappa})\sin((\kappa/\kappa_0)\psi)$$
$$+ \mathrm{Im}\,(S^1_{\boldsymbol{m},\kappa})\cos((\kappa/\kappa_0)\psi). \qquad (65)$$

Proof. See Appendix B.   □

Fixed points of the reduced dynamics in polar coordinates correspond to periodic orbits of the full system as the SSM is a time-periodic invariant manifold, i.e., $\boldsymbol{z(t)} = \boldsymbol{W}_\varepsilon(\boldsymbol{p}(t), \phi)$. As statement (ii) of Lemma 5 only requires the computation of zero level sets, the forced response can be computed independently for each forcing frequency $\{\Omega_1, \ldots \Omega_z\}$ in the interval of interest. Another consequence is that isolated regions of forced response, the so-called *isolas*, can be computed at the same time. This is in stark contrast to continuation-based methods, which will only find such branches of response from initial conditions that are specified close to isolas.

B. Computational complexity

We already discussed the basic steps and their associated computational complexity for computing FRCs via the SSM-based ROM and via full-system collocation in Sec. V B. There, we noted that steps 2–3 in SSM computation were fully parallelizable. However, step 4 employed numerical continuation of the reduced dynamics via collocation and, hence, was not parallelizable. Thanks to Lemma 5, the periodic response computation is now reduced to a fixed-point calculation that can be parallelized over the frequency domain of interest. This makes the proposed SSM routine fully parallelizable. We update step 4 and the associated computational complexity due to Lemma 5 in Table VII (see Appendix C 3).

C. Examples

We make use of Lemma 5 to analyze the forced response of dynamical systems that are subject to direct and parametric excitation simultaneously. In our examples, we will consider systems of the form

$$M\ddot{\boldsymbol{y}} + C\dot{\boldsymbol{y}} + \left(\boldsymbol{K} + \varepsilon\mu\boldsymbol{Q}\cos(2\Omega t)\right)\boldsymbol{y} + \boldsymbol{f}(\boldsymbol{y}, \dot{\boldsymbol{y}}) = \varepsilon\boldsymbol{g}(\boldsymbol{y}, \dot{\boldsymbol{y}}, \Omega t), \quad (66)$$

with the function $\boldsymbol{g}$ including nonlinear parametric excitation and external excitation. Solving the invariance equation (17) up to $\mathcal{O}(\varepsilon)$ provides a parametrization of the nonautonomous SSM. The computation of these parametrizations and the extraction of the FRCs will be performed with SSMTool 2.4. For a given dynamical system of first or second order, the algorithm automatically solves the invariance equations (23) and (31) up to any desired order and computes the steady states using Lemma 5.

1. Self-excited parametric oscillator

Self-excitation of mechanical systems is caused by negative linear damping that leads to a destabilization of the trivial fixed point of the linearized system. In contrast, nonlinear positive damping stabilizes the system for large oscillation amplitudes and forms a limit cycle, resulting in behavior described by a Hopf-type normal form.[69] Such self-excitations may arise, for instance, from dry friction, vibrations during machine cutting, or nonlinear feedback control in MEMS devices.[70–72]

The example we study here represents a 2-DOF oscillator with nonlinear elasticity and damping, as shown in Fig. 8. This system is subject to external excitation along one DOF, which is coupled to the second DOF via a spring with periodically varying stiffness (see, e.g., Szabelski and Warminski[23,73]). The three types of excitation seen in
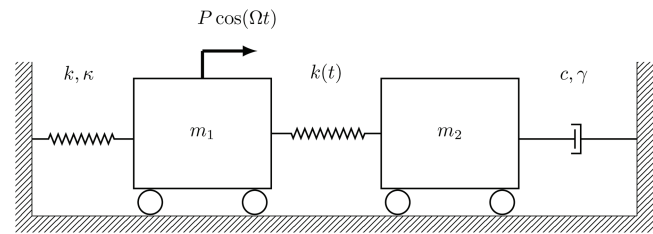
FIG. 8. Model of a self-excited oscillator system with external and parametric excitation. The stiffness of the coupling spring varies periodically as $k(t) = 4k(1 + \mu\cos(2\Omega t))$. External excitation is introduced via the term $P\cos(\Omega t)$. The negative linear damping coefficient c introduces self-excitation that is stabilized by the nonlinear damping with coefficient γ. The left spring is characterized by linear and nonlinear stiffness coefficients k and κ.

this example (external, parametric, and self-excitation) are present in a number of engineered structures, including coupled vibrations of unbalanced shafts with time-varying rigidity, whirling in slide bearings, and metal machine cutting. To study the system dynamics, the cited references construct approximate analytical solutions by assuming a steady state in the form of a sum of trigonometric functions. Assuming that the oscillation amplitudes vary slowly in time and, therefore, dropping higher-order derivatives, the authors arrive at an expression for the amplitudes, which they solve numerically. The equations of motion can be written in the dimensionless form[23]

$$\ddot{y}_1 + \tilde{k}(1 - \tilde{\mu}\cos 2\Omega t)(y_1 - y_2) + y_1 + \tilde{\kappa}y_1^3 = \tilde{P}\cos\Omega t, \quad (67)$$

$$\ddot{y}_2 - (\tilde{c} - \tilde{\gamma}\dot{y}_2^2)\dot{y}_2 - \tilde{k}M(1 - \tilde{\mu}\cos 2\Omega t)(y_1 - y_2) = 0. \quad (68)$$

The parameters values are chosen as $\tilde{k} = 4, \tilde{\mu} = 0.2, \tilde{\kappa} = 0.1, \tilde{c} = 0.01, \tilde{\gamma} = 0.05, M = 0.5, \tilde{P} = 0.2$, and $\varepsilon = 1$, where $(\tilde{\bullet})$ represents a dimensionless variant of the corresponding physical quantity $(\bullet)$ shown in Fig. 8. Using SSM theory to obtain the FRC of this dynamical system involves the following steps.

1. System setup: Using the standardized form (1), systems (67) and (68) can be rewritten as

$$\boldsymbol{M} = \begin{pmatrix} 1 & 0 \\ 0 & 1 \end{pmatrix}, \quad \boldsymbol{K} = \begin{pmatrix} \tilde{k}+1 & -\tilde{k} \\ -\tilde{k}M & \tilde{k}M \end{pmatrix}, \quad (69)$$

$$\boldsymbol{Q} = \tilde{k}\begin{pmatrix} -1 & 1 \\ M & -M \end{pmatrix}, \quad \boldsymbol{C} = \begin{pmatrix} 0 & 0 \\ 0 & -\tilde{c} \end{pmatrix}, \quad (70)$$

$$\boldsymbol{f}(\boldsymbol{y}, \dot{\boldsymbol{y}}) = \begin{pmatrix} \tilde{\kappa}y_1^3 \\ \tilde{\gamma}\dot{y}_2^3 \end{pmatrix}, \quad \boldsymbol{g}(\Omega t) = \tilde{P}\begin{pmatrix} \cos\Omega t \\ 0 \end{pmatrix}. \quad (71)$$

To solve the invariance equations, we expand the nonlinearity and forcing in Taylor and Taylor–Fourier series. Details on this procedure can be found in Appendix A 1.

2. Choose master subspace: Linear analysis of the corresponding first-order ODE (6) provides the eigenvalue pairs $\lambda_1, \overline{\lambda_1} \approx 0.0013 \pm 2.5887i$ and $\lambda_2, \overline{\lambda_2} \approx 0.0037 \pm 0.5463i$. We choose to analyze the resonant excitation of the first mode with excitation frequency values $\Omega \approx \text{Im }\lambda_1$ and construct a time-periodic SSM over the spectral subspace $\mathscr{E} = \{\boldsymbol{v}_1, \overline{\boldsymbol{v}_1}\}$.

(a)

(b)
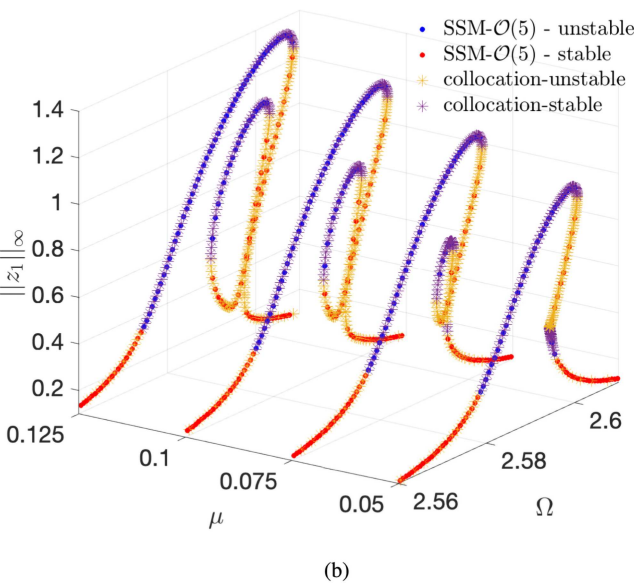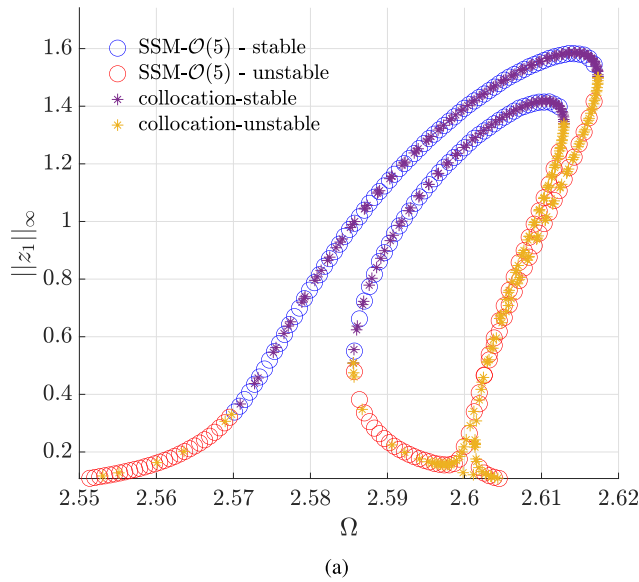
FIG. 9. (a) Forced response curve of the self-excited oscillator for a parametric excitation amplitude of $\mu = 0.2$. The forced response obtained from a fifth-order approximation of the dynamics on the non-autonomous SSM accurately describes the full-system response. Results are verified using po-toolbox of COCO. (b) Variation in the forced response for different amplitudes of parametric excitation while keeping the external excitation amplitude constant.

3. Autonomous SSM and reduced dynamics: The leading-order autonomous cohomological equation is solved by choosing

$$W_{e_1} = v_1, \ W_{e_2} = \overline{v_1}, \tag{72}$$

$$R_{e_1} = \begin{pmatrix} \lambda_1 \\ 0 \end{pmatrix}, \ R_{e_2} = \begin{pmatrix} 0 \\ \lambda_1 \end{pmatrix}. \tag{73}$$

Subsequently, the autonomous cohomological equation (27) can be solved recursively to the desired order. Near-resonances between the master modes of the type (28) are detected automatically and the autonomous reduced dynamics are transformed to their normal form accordingly.

4. Assemble non-autonomous cohomological equations: The autonomous SSM and reduced dynamics coefficients do not depend on the external excitation frequency. As this is not the case for non-autonomous coefficients, the nonautonomous cohomological equation has to be solved for every forcing frequency Ω. Given a set of forcing frequencies $\{\Omega_1, \ldots, \Omega_z\}$, the nonautonomous cohomological equation is solved up to the desired order independently for each frequency. Near-resonances in the master subspace of the form (36) are automatically detected at each order of computation, which determines the nontrivial coefficients of the reduced vector field according to a normal form style of parametrization. The coefficients of the reduced dynamics are used to construct the function $r(\rho, \psi, \Omega)$ defined in Eq. (55), whose zero level set provides us the forced response according to Lemma 5. The resulting reduced dynamics up to cubic order at frequency $\Omega = 2.6$ rad/s can be written as

$$\dot{p} = (1328.6 + 25\,887.3i)p + (-35.9 + 63.2i)p^2\bar{p}$$
$$+ (7.4 + 1152.5i)e^{2i\phi}\bar{p} + (0.2 - 0.8i)e^{-i\phi}p^2$$
$$+ (-0.4 + 1.6i)e^{i\phi}p\bar{p} + (1 - 1.4i)e^{-2i\phi}p^3, \tag{74}$$

where we have used a rescaled time variable $s = 10^{-4}t$ and defined the phase variable $\phi = \Omega t$. The dynamics along the second reduced coordinate is simply given by the complex conjugate of (74).

Figure 9(a) shows the FRC obtained from this procedure, where we observe a self-intersecting loop in the FRC. Once again, we verified the SSM-based reduced results against the full system using the po-toolbox of COCO, where the relevant continuation parameters were set according to Table X in Appendix C. The computation time for this self-excited oscillator using a sequential implementation of the non-autonomous SSM computation is 58 s. Meanwhile, the verification via continuation on the full system takes 66 s. We observe that in this sequential implementation on a low-dimensional example, the ROM does not bring any significant computational savings relative to the full system in this low-dimensional example. In Fig. 9(b), we investigate the relative effects of the parametric and excitation on the system's response. We observe that, as the amplitude of the parametric excitation is decreased for a fixed external excitation amplitude, the size of the self-intersecting loop attached to the main branch of the FRC also decreases. We refer to Szabelski and Warminski[22,23] for an extensive discussion of this phenomenon.

Similar oscillator systems featuring self-excitation or parametric amplification have been shown to exhibit complicated forced response curves, including isolated branches of response.[20,73] To

22 July 2024 13:58:33

demonstrate the effectiveness of SSM-based ROMs in reproducing such complicated forced response curves, we have implemented further examples of self-excited oscillators with isolas[73] and parametric amplifiers with nonlinear damping.[20] These examples are openly available in SSMTool.[62] Next, we discuss finite-element-type examples under parametric and external excitation.

2. Bernoulli beam with parametric and external excitation

We now return to the nonlinear Bernoulli beam example with the parameters listed in Table I. In addition to the parametric excitation, however, the free end is now forced externally as well. The resulting equations of motion for the discretized variables are now given by

$$M\ddot{y} + C\dot{y} + Ky + \varepsilon\mu\cos 2\Omega t Qy + f(y, \dot{y}) = \varepsilon f_{ext}^0 \cos(\Omega t). \quad (75)$$

Here, $f(y, \dot{y})$ again includes the nonlinear damping coefficient γ of the damper, as well as the nonlinear stiffness κ of the spring attached to the tip of the beam. Once again, $Q \in \mathbb{R}^{n \times n}$ is a Boolean matrix that performs projection onto the transverse degree of freedom at the tip of the beam. The harmonic external excitation vector f_{ext}^0 acts on the tip of the beam, with a unit magnitude in the transverse direction. The damping coefficient is set to $\sigma = 1$. The external excitation amplitude and the relative parametric excitation amplitude are taken to be $\varepsilon = 2 \times 10^{-3}$ and $\mu = 45$ (mN/mm), respectively. The system is forced in resonance with the first mode with the eigenvalue pair

$$\lambda_1, \overline{\lambda_1} \approx -0.1238 \pm 6.9995i. \quad (76)$$

The excitation frequencies for parametric and external excitation are assumed to have a 2:1 relationship. Therefore, the direct forcing is resonant with the first eigenmode of the beam, whereas the parametric term is operated in the regime of principal parametric resonance. Figure 10(a) shows the forced response for a 20 element model with $n = 40$ DOFs, where we observe an isolated branch of forced response under the main branch for the chosen parameter values. The emergence of such an isola with an increasing parametric excitation amplitude μ has been studied in systems where parametric resonance and external excitation interact. Indeed, this isola is associated with the coexistence of the two resonances, i.e., the parametric 2:1 resonance and the direct 1:1 resonance of the external excitation with the eigenvalues of the first mode.[12,25]

We verify the FRC obtained from the SSM-based ROM against the full-system collocation implemented using the po toolbox of COCO with parameters set according to Table X. The isolated branch of the forced response, which appears inside the main branch of the FRC, is not detected by the continuation run. We use an initial solution on the isola provided by the SSM-based ROM as an input for COCO to independently verify the isolated branch for the full system. The verification of the main branch took a total of 4 h and 40 min, while the isolated response needed 15 h and 17 min. At the same time, using Lemma 5, the SSM-based ROM takes only 48 s for FRC extraction with a sequential implementation.

Next, we repeat our analysis for larger system sizes resulting from higher-order discretizations of the beam. The corresponding computation times are depicted in Fig. 11. All computations for this
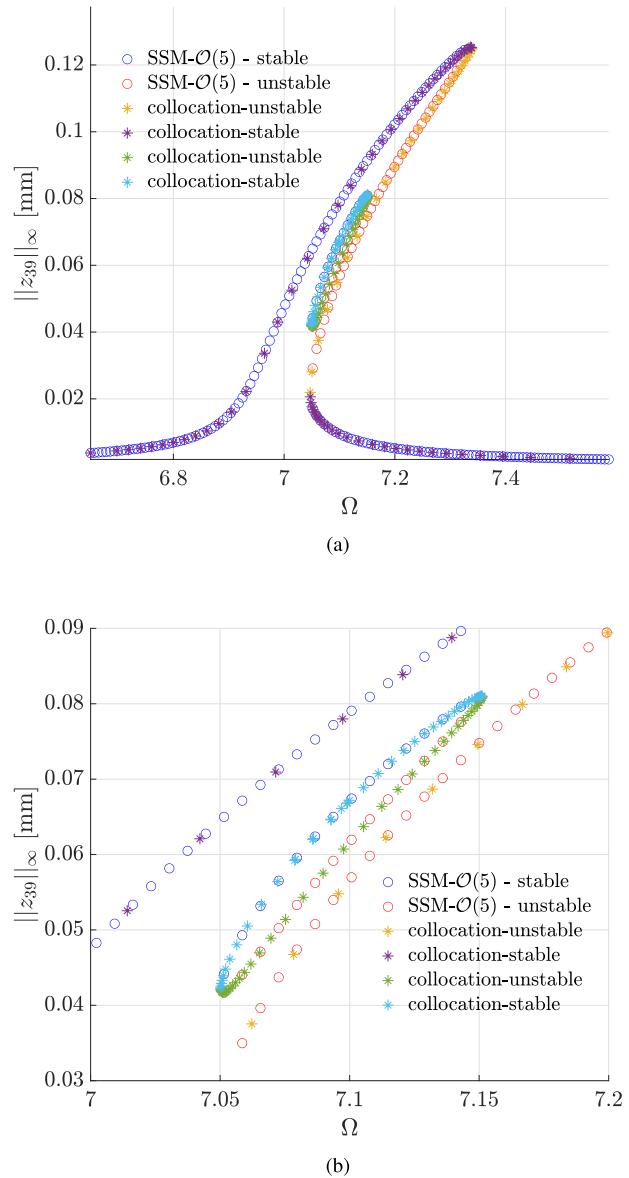
FIG. 10. (a) Forced response obtained for the externally excited Bernoulli beam with periodically varying stiffness actuation at the tip, reported at the transverse DOF, z_{39}, located at the tip of the beam ($n = 40$). The nonlinear spring attached to the beam leads to a hardening-type response. Due to the interplay of external and parametric excitation, an isola arises for sufficiently large values of the parametric excitation amplitude μ [$\mu = 45$ (mN/mm) for this simulation]. The isola is independently verified using an initial condition provided by the results of the SSM computation. (b) Close-up view of the isolated response branch verified against the full system in a separate continuation run.

example were performed on the Euler Cluster of ETH Zürich due to the long runtimes of the collocation routine. We increased the system size up to 25 000 elements, resulting in up to $n = 50\,000$ DOFs. The sequential computation of the FRC, including the repeated
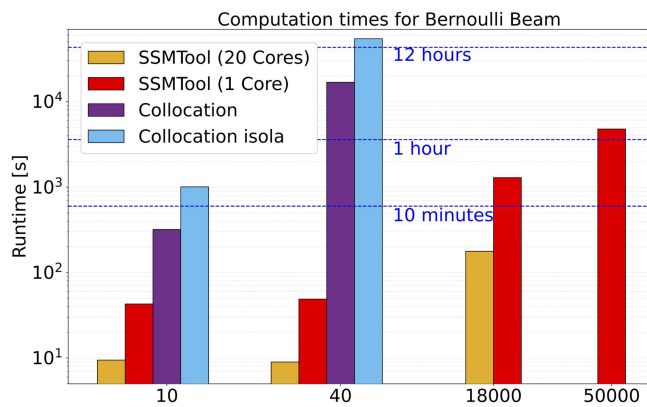
FIG. 11. Computation times for the FRC of the externally excited Bernoulli beam example. Results from the SSM-based ROMs were verified against the full system using the `po`-toolbox of `COCO` (see Fig. 10). Computation for isolas in the forced response is reported separately as they were verified in independent continuation runs.

computation of the non-autonomous SSM and its reduced dynamics for each forcing frequency $\{\Omega_1, \ldots, \Omega_z\}$, now takes 1 h and 19 min.

VII. CONCLUSION

We have developed an algorithm for computing non-autonomous primary SSMs and their reduced dynamics up to any desired order of accuracy in externally and parametrically forced systems. In doing so, we have taken into account prior developments and extended them to the case of parametrically excited mechanical systems with nonlinearities of arbitrary order and magnitude, including nonlinear damping. We have put forward automated routines for computing primary SSMs for second-order mechanical systems, in particular, and first-order dynamical systems, in general. In our derivations and computations, we have made use of the multi-index notation for the expansions and carried out computations in physical coordinates using minimal eigenvectors of the full system. All this optimizes memory requirements and avoids modal transformations that are computationally infeasible for high-dimensional systems.

Using the SSM-reduced models as the basis for parameter continuation, we have shown how to compute the stability diagrams for the principal resonance of periodic, parametrically excited systems. Furthermore, we have shown that in systems under additional external excitation, the forced response can be obtained by simply locating the zeros of a two-dimensional function, i.e., without numerical continuation. As a result, it is now possible to parallelize the computation of the periodic responses attached to two-dimensional, nonautonomous SSMs for systems subject to periodic external and parametric excitation over any desired range of forcing frequencies. All these algorithms and their applications to our examples are available in the open-source package `SSMTool 2.4`.[62]

With examples treating coupled Mathieu equations, a parametrically excited Bernoulli beam, and an axially forced prismatic beam, we have illustrated how SSM-based model reduction can be

used to obtain accurate stability diagrams and FRCs in parametrically excited systems at a significantly reduced computational cost. Indeed, we analyzed a number of typical low-dimensional models studied previously in the literature and showed that SSM-based ROMs provide accurate predictions even if they do not necessarily yield computational savings. In contrast, SSM-reduced models also provide major computational advantages over the full system in more complex examples such as a Bernoulli beam attached to a nonlinear damper and spring and subject to external and parametric excitation. In that example, we have uncovered an internal isola, which is an effect that has been observed for one-dimensional models subject to parametric resonance and external excitation.[12,25] Ours appears to be the first demonstration of this phenomenon in finite-element models. We showcased the power of this mathematically grounded SSM reduction by increasing system sizes beyond the capabilities of collocation-based continuation methods when applied to the full system. We also demonstrated how parallelization can be used to reduce the computation time by an order of magnitude in SSM-based FRC calculations.

Future work may target systems with even higher dimensionality, where the beneficial effects of model reduction should weigh in even more stunningly. Areas of related applications include various types of parametrically driven MEMS devices, such as comb-driven micromirrors, among others.[8,9,11] Additionally, the developments presented here open the door for an in-depth analysis of the interaction of more complex time-dependent phenomena, such as parametric resonance in MEMS systems with internal resonances.[74]

AUTHOR DECLARATIONS

Conflict of Interest

The authors have no conflicts to disclose.

Author Contributions

Thomas Thurnher: Formal analysis (lead); Methodology (lead); Software (lead); Validation (lead); Writing – original draft (lead). **George Haller:** Conceptualization (supporting); Writing – review & editing (equal). **Shobhit Jain:** Conceptualization (lead); Formal analysis (supporting); Methodology (supporting); Supervision (lead); Writing – review & editing (equal).

DATA AVAILABILITY

The code used to generate the numerical results included in this paper is available as part of the open-source package SSMTool, at https://doi.org/10.5281/zenodo.4614201, Ref. 62.

APPENDIX A: SSM COMPUTATION IN MULTI-INDEX FORMAT

In this section of the appendix, we provide the mathematical details for SSM computations in physical coordinates with the use

of multi-indices, including the proofs for Lemmas 1–4. We begin by reviewing the multi-index formalism and its advantages. We then give an in-depth derivation of the expressions that determine the SSM and its reduced dynamics parametrizations. We present these results for second- and first-order ODEs.

1. Multi-index calculus

A multi-index of order $m \in \mathbb{N}$ is a vector $\boldsymbol{m} \in \mathbb{N}^M$ such that $||\boldsymbol{m}||_1 = m$. The unit multi-indices with a single nonzero entry in the jth position are denoted by $\boldsymbol{e}_j$. The addition and subtraction of multi-indices are defined element-wise. Using multi-indices, multivariate monomials can be conveniently expressed as

$$\boldsymbol{p^m} = p_1^{m_1} \cdots p_M^{m_M}. \tag{A1}$$

Likewise, a time derivative of such monomials is conveniently expressed as

$$\frac{d\boldsymbol{p^m}}{dt} = \sum_{j=1}^{M} \partial_{p_j}\boldsymbol{p^m}\dot{p}_j = \sum_{j=1}^{M} m_j \boldsymbol{p^{m-e_j}}\dot{p}_j. \tag{A2}$$

a. Composition coefficients

In SSM computations, composition of nonlinear forces with the nonlinear SSM parametrization has to be performed. For this, we need to compute scalar powers s of power series written in multi-index notation, i.e., $(\sum_m W_m^i \boldsymbol{p^m})^s$. A convenient method, which offers a recursive definition of the resulting coefficients, uses the concept of radial derivative discussed by Haro *et al.*[48] Ponsioen *et al.*[60] use this method to express the coefficients $H_{s,\boldsymbol{h}}$ in the expansion

$$\left(\sum_m W_m^i \boldsymbol{p^m}\right)^s = \sum_{\boldsymbol{h}} H_{s,\boldsymbol{h}}^i \boldsymbol{p^h} \tag{A3}$$

using the recursive definition

$$H_{s,\boldsymbol{h}}^i = \frac{s}{h_j} \sum_{\boldsymbol{m} \leq \boldsymbol{h}} m_j W_m^i H_{s-1,\boldsymbol{h-m}}^i, \tag{A4}$$

where j is the index of the smallest nonzero element in $\boldsymbol{h}$. To simplify the calculation of this recursion, it is useful to look at some special cases under the assumption that the coefficients W_m^i are the autonomous coefficients of the ith coordinate of the SSM expansion. The SSM parametrization does not contain constant terms, which means that all composition coefficients are zero for $|\boldsymbol{m}| = 0$. The properties of $H_{s,\boldsymbol{h}}^i$ are then

- $H_{1,\boldsymbol{0}}^i = 0$,
- $H_{1,\boldsymbol{h}}^i = W_{\boldsymbol{h}}^i$,
- $H_{0,\boldsymbol{h}}^i = 0$ for all $\boldsymbol{h} \neq \boldsymbol{0}$,
- $H_{0,\boldsymbol{0}}^i = 1$.

We generalize this concept to vector-valued power series by collecting all terms corresponding to the same multi-index $\boldsymbol{h} \in \mathbb{N}^M$ and

defining a new composition coefficient $H_{\boldsymbol{n},\boldsymbol{h}}$ such that

$$\left(\sum_{\boldsymbol{m} \in \mathbb{N}^M} W_m \boldsymbol{p^m}\right)^{\boldsymbol{n}} = \prod_{i=1}^{N} \left(\sum_{\boldsymbol{m} \in \mathbb{N}^M} W_m^i \boldsymbol{p^m}\right)^{n_i} \tag{A5}$$

$$= \prod_{i=1}^{N} \left(\sum_{\boldsymbol{u} \in \mathbb{N}^M} H_{n_i,\boldsymbol{u}}^i \boldsymbol{p^u}\right) \tag{A6}$$

$$= \sum_{\boldsymbol{h} \in \mathbb{N}^M} H_{\boldsymbol{n},\boldsymbol{h}} \boldsymbol{p^h}. \tag{A7}$$

In more detail,

$$H_{\boldsymbol{n},\boldsymbol{h}} := \sum_{\boldsymbol{u}_1 \in \mathbb{N}^M} \cdots \sum_{\boldsymbol{u}_{2n} \in \mathbb{N}^M} H_{n_1,\boldsymbol{u}_1}^1 \cdots H_{n_{2n},\boldsymbol{u}_{2n}}^{2n} \bigg|_{\sum \boldsymbol{u}_i = \boldsymbol{h}}. \tag{A8}$$

Although a vectorization of this computation provides a very efficient routine for the composition of power series, it also poses a major bottleneck in terms of memory and time requirements in the SSM computation proposed here.

b. Redundancy in tensor notation

We now discuss the computational disadvantages of a tensor-based notation compared to the use of multi-indices. Let $\boldsymbol{p} \in \mathbb{C}^2$ and consider the Taylor expansion of a nonlinear function $\boldsymbol{W}(\boldsymbol{p})$ in the tensor notation as

$$\boldsymbol{W}(\boldsymbol{p}) = \sum_{i \in \mathbb{N}} \boldsymbol{W}_i \boldsymbol{p}^{\otimes i}. \tag{A9}$$

Specifically, the second term in the expansion (A9) can be represented by a 2×4 matrix $\boldsymbol{W}_2$ acting on the Kronecker product $\boldsymbol{p} \otimes \boldsymbol{p}$ as

$$\boldsymbol{W}_2 \boldsymbol{p} \otimes \boldsymbol{p} = \begin{bmatrix} W_{11} & W_{12} & W_{13} & W_{14} \\ W_{21} & W_{22} & W_{23} & W_{24} \end{bmatrix} \begin{bmatrix} p_1 p_1 \\ p_1 p_2 \\ p_2 p_1 \\ p_2 p_2 \end{bmatrix} \tag{A10}$$

$$= \begin{bmatrix} W_{11}p_1^2 + (W_{12} + W_{13})p_1 p_2 + W_{14}p_2^2 \\ W_{21}p_1^2 + (W_{22} + W_{23})p_1 p_2 + W_{24}p_2^2 \end{bmatrix}. \tag{A11}$$

Examining Eq. (A11), we note that only six of the eight coefficients contained in the matrix $\boldsymbol{W}_2$ are needed to uniquely represent $\boldsymbol{W}_2 \boldsymbol{p} \otimes \boldsymbol{p}$. Indeed, the same term in multi-index notation,

$$\boldsymbol{W}(\boldsymbol{p}) = \sum_{\boldsymbol{m} \in \mathbb{N}^M} \boldsymbol{W}_m \boldsymbol{p^m}, \tag{A12}$$

is characterized by six unique multi-index coefficients given as

$$\boldsymbol{W}_{\binom{2}{0}} = \begin{bmatrix} W_{11} \\ W_{21} \end{bmatrix}, \quad \boldsymbol{W}_{\binom{1}{1}} = \begin{bmatrix} W_{12} + W_{13} \\ W_{22} + W_{23} \end{bmatrix}, \quad \boldsymbol{W}_{\binom{0}{2}} = \begin{bmatrix} W_{13} \\ W_{23} \end{bmatrix}. \tag{A13}$$

This redundancy in the number of coefficients utilized by the tensor notation relative to the multi-index notations grows with the order of expansion. Consider, for instance, the case of a two-dimensional SSM, where, at any order Γ, the expansion is characterized by a tensor with $N2^{\Gamma+1}$ coefficients. However, we have only $\Gamma + 1$ unique

monomials associated with these coefficients. Hence, while the number of unique monomials grows linearly with the order Γ, the corresponding number of tensor coefficients grows exponentially in Γ.

We remark, however, that the tensors can be specially constructed to contain only a minimal number of nonzero coefficients equal to that in the multi-index notation. This is possible by exploiting the inherent symmetries in monomials associated with the expansion, e.g., by using a sparse or symmetric definition of tensor arrays. In practice, the SSM coefficients that are determined numerically by solving invariance equations may still lead to densely populated or asymmetric tensor arrays. At each order of computation, the computed coefficients would, therefore, require recasting to this minimal form, resulting in unnecessary computational overhead.

Furthermore, it turns out that the cohomological equations (27) and (35) that need to be solved for SSM expansion coefficients are decoupled for individual multi-indices. For computing a two-dimensional autonomous SSM at order Γ in a vectorized tensor-based notation adopted in Ref. 34, a linear system of dimension $N2^{\Gamma+1}$ needs to be solved. Using multi-indices instead, only $\Gamma + 1$ linear systems of dimension n each need to be solved. One can also solve the linear systems associated with each tensor index independently, as remarked in Ref. 34 and as done for second-order systems in Refs. 53 and 61. In that case, a total of $2^{\Gamma+1}$ systems of linear equations of dimension n must be solved in the tensor-index notation. Hence, for two-dimensional SSMs, the use of multi-indices leads to an exponential decrease in the number of linear systems that needs to be solved relative to the tensor notation as the expansion order increases.

Thus, we have shown the tensor notation results in redundant computational costs relative to the multi-index notation.

c. Examples of nonlinear force expansion

We expand the excitation and nonlinearity in the multi-index notation as

$$f(y, \dot{y}) = \sum_{a,b \in \mathbb{N}^n} f_{a,b} y^a \dot{y}^b, \qquad (A14)$$

$$g(y, \dot{y}, \phi) = \sum_{a,b \in \mathbb{N}^n} \sum_{\kappa \in \mathbb{Z}^K} g_{a,b,\kappa} e^{i\langle \kappa, \phi \rangle} y^a \dot{y}^b, \qquad (A15)$$

where the coefficients $f_{a,b}$, $g_{a,b,\kappa} \in \mathbb{C}^n$. Note that these coefficients can be recast in a first-order form simply by associating a multi-index $n \in \mathbb{N}^N$ to each pair a, b such that in the phase space, $z^n = y^a \dot{y}^b$. The first-order version of the two expansions (A14) and (A15) can then be written as

$$F(z) = \sum_{n \in \mathbb{N}^N} F_n z^n, \quad F_{\binom{a}{b}} = \begin{bmatrix} f_{a,b} \\ 0_n \end{bmatrix}, \qquad (A16)$$

$$G(z, \phi) = \sum_{n \in \mathbb{N}^N} \sum_{\kappa \in \mathbb{Z}^k} G_{n,\kappa} e^{i\langle \kappa, \phi \rangle} z^n, \quad G_{\binom{a}{b}, \kappa} = \begin{bmatrix} g_{a,b,\kappa} \\ 0_n \end{bmatrix}. \qquad (A17)$$

As an example of the above notation, we consider the forcing in the self-excited oscillator system (67) and (68). The forcing term

contains external and linear parametric excitation given by

$$g(\Omega t, y) = \cos \Omega t \begin{pmatrix} q \\ 0 \end{pmatrix} + \lambda \cos 2\Omega t \begin{pmatrix} y_1 - y_2 \\ -M(y_1 - y_2) \end{pmatrix} \qquad (A18)$$

$$= (e^{i\Omega t} + e^{-i\Omega t}) \begin{pmatrix} q/2 \\ 0 \end{pmatrix} + (e^{i2\Omega t} + e^{-i2\Omega t}) \frac{\lambda}{2}$$

$$\times \begin{pmatrix} y_1 - y_2 \\ -M(y_1 - y_2) \end{pmatrix}. \qquad (A19)$$

Here, the set of harmonics is given as $K = \{1, -1, 2, -2\}$. As the system contains only two DOFs, the spatial multi-indices are two dimensional and the vectors $g_{n,\kappa}$ that characterize the expansion (A15) are given as

$$g_{0,1} = g_{0,-1} = \begin{pmatrix} q/2 \\ 0 \end{pmatrix}, \qquad (A20)$$

$$g_{e_1,2} = g_{e_1,-2} = \begin{pmatrix} \lambda/2 \\ -M\lambda/2 \end{pmatrix}, \qquad (A21)$$

$$g_{e_2,2} = g_{e_2,-2} = \begin{pmatrix} -\lambda/2 \\ M\lambda/2 \end{pmatrix}. \qquad (A22)$$

2. Second-order computation

a. Autonomous SSM computation

In order to compute the SSMs and their reduced dynamics parametrizations for second-order mechanical systems, we express them as Taylor series (24)–(26). Substituting these expansions into the autonomous invariance equation (23) and collecting unique monomial terms, we obtain the system (27) of the linear equations for each multi-index m as we detail below. At the leading order, i.e, for monomial multi-index p^{e_i}, we obtain

$$\begin{bmatrix} C & M \\ M & 0 \end{bmatrix} \sum_{j=1}^{M} \begin{bmatrix} w_{e_j} \\ \dot{w}_{e_j} \end{bmatrix} R_{e_i}^j = \begin{bmatrix} -K & 0 \\ 0 & M \end{bmatrix} \begin{bmatrix} w_{e_i} \\ \dot{w}_{e_i} \end{bmatrix}. \qquad (A23)$$

Eliminating the velocity variables $\dot{w}_{e_i}$ from system (A25), we obtain

$$M \sum_{j=1}^{M} \sum_{k=1}^{M} w_{e_k} R_{e_j}^k R_{e_i}^j + C \sum_{j=1}^{M} w_{e_j} R_{e_i}^j + K w_{e_i} = 0. \qquad (A24)$$

From the eigenvalue problem (12), we note that the choice $w_{e_j} = \phi_j$ and $R_{e_j}^j = \delta_{ij} \lambda_i$ solves Eq. (A24). Together with Eq. (A23), this solution choice for the leading-order displacement parametrization implies that $\dot{w}_{e_i} = \phi_i \lambda_i$. Higher-order terms of the invariance equation (23) for a multi-index m are given as

$$\left(\begin{bmatrix} -K & 0 \\ 0 & M \end{bmatrix} - \Lambda_m \begin{bmatrix} C & M \\ M & 0 \end{bmatrix} \right) \begin{bmatrix} w_m \\ \dot{w}_m \end{bmatrix}$$

$$= \sum_{j=1}^{M} \begin{bmatrix} C & M \\ M & 0 \end{bmatrix} \begin{bmatrix} \phi_j \\ \phi_j \lambda_j \end{bmatrix} R_m^j + \begin{bmatrix} 1 & 0 \\ 0 & M \end{bmatrix} \begin{bmatrix} Y_m \\ V_m \end{bmatrix}, \qquad (A25)$$

where we define

$$\Lambda_m := \Lambda \cdot m, \qquad (A26)$$

$$Y_m := \sum_{j=1}^{M} \sum_{\substack{u,k \in \mathbb{N}^M \\ 1 < u < m \\ u+k-e_j=m}} (M\dot{w}_u) u_j R_k^j + CV_m - \sum_{n \in \mathbb{N}^N} f_n H_{n,m}, \quad (A27)$$

$$V_m := \sum_{j=1}^{M} \sum_{\substack{u,k \in \mathbb{N}^M \\ 1 < u < m \\ u+k-e_j=m}} w_u u_j R_k^j. \quad (A28)$$

We rewrite the second set of equations in system (A25) to obtain an explicit expression for the velocity parametrization as

$$\dot{w}_m = \Lambda_m w_m + \sum_{j=1}^{M} \phi_j R_m^j + V_m. \quad (A29)$$

The velocity parametrization depends purely on multiplicative terms of the displacement parametrization and the reduced dynamics. Indeed, the expression (A29) is identical to the general result of Lemma 2, which we prove later. Now we utilize relation (A29) to rewrite Y_m in terms of the displacement parametrization and substitute the resulting expression into the first set of equations in system (A25) to obtain

$$\overbrace{\left(K + \Lambda_m C + (\Lambda_m)^2 M\right)}^{=:L_m} w_m = D_m R_m + C_m, \quad (A30)$$

where $C_m := -\Lambda_m M V_m - Y_m$ and $D_m \in \mathbb{C}^{n \times M}$ is a matrix whose jth column is given by $(D_m)_j := -((\Lambda_m + \lambda_j)M + C)\phi_j$ for every $j = 1, \ldots, M$. This concludes the proof of Lemma 1.

Now we prove Lemma 2 by applying the chain rule to compute the velocity parametrization and using the fact that the autonomous reduced dynamics trajectories satisfy $\dot{p} = R(p)$. Finally, we collect the terms that sum up to the same multi-index m as

$$\dot{w}_m = \frac{dw}{dt}\bigg|_m = [Dw(p)\dot{p}]_m = [Dw(p)R(p)]_m \quad (A31)$$

$$= \sum_{j=1}^{M} \sum_{\substack{u,k \in \mathbb{N}^M \\ u+k-e_j=m}} w_u u_j R_k^j. \quad (A32)$$

Indeed, Eq. (A32) can be verified against the results from the standard invariance equation given in Eq. (A29).

a. Reduced dynamics. The linear system (27) contains n equations for each multi-index m with n unknowns associated with the displacement parametrization w_m and additional M unknowns associated with the reduced dynamics parametrization R_m. This underdeterminacy of system (27) allows different solution choices for the reduced dynamics parametrization. Specifically, a normal-form style parametrization is appealing when (near)-resonances are present among the master subspace eigenvalues. Indeed, for an eigenvalue

λ_i associated with the master subspace, a near-resonance of the form

$$\lambda_i \approx \Lambda_m \quad (A33)$$

results in the coefficient matrix L_m being nearly singular. To ensure (robust) solvability of system (27), the coefficients R_m must be chosen such that the right-hand side of system (27) is orthogonal to the (near) kernel of L_m. In particular, we require (see, e.g., Refs. 34 and 48)

$$\theta_i^*\left(K + \Lambda_m C + (\Lambda_m)^2 M\right)w_m = 0, \quad (A34)$$

which directly provides us the essentially nonzero reduced dynamics coefficients R_m^i in the normal-form parametrization style as

$$\theta_i^*((\Lambda_m + \lambda_i)M + C)\phi_i R_m^i = -\theta_i^*(\Lambda_m M V_m + Y_m). \quad (A35)$$

b. Non-autonomous SSM

Collecting terms at $\mathcal{O}(\varepsilon)$ in the invariance equation (17) corresponding to a given monomial multi-index m and Fourier harmonic κ, we obtain

$$\left(\begin{bmatrix} -K & 0 \\ 0 & M \end{bmatrix} - \Lambda_{m,\kappa}\begin{bmatrix} C & M \\ M & 0 \end{bmatrix}\right)\begin{bmatrix} x_{m,\kappa} \\ \dot{x}_{m,\kappa} \end{bmatrix}$$
$$= \sum_{j=1}^{M} \begin{bmatrix} C & M \\ M & 0 \end{bmatrix}\begin{bmatrix} \phi_j \\ \phi_j \lambda_j \end{bmatrix} S_{m,\kappa}^j + \begin{bmatrix} 1 & 0 \\ 0 & M \end{bmatrix}\begin{bmatrix} Y_{m,\kappa} \\ V_{m,\kappa} \end{bmatrix}, \quad (A36)$$

where we define

$$\Lambda_{m,\kappa} := \Lambda_m + i\langle\Omega,\kappa\rangle, \quad (A37)$$

$$Y_{m,\kappa} := M\sum_{j=1}^{M} \sum_{\substack{u,k \in \mathbb{N}^M \\ u+k-e_j=m \\ |k|<m}} \left(\dot{w}_u u_j S_{k,\kappa}^j + \dot{x}_{k,\kappa} k_j R_u^j\right) + CV_{m,\kappa}$$

$$- \sum_{n \in \mathbb{N}^N} f_n \sum_{j=1}^{2n} n_j\left(\sum_{\substack{u,h \in \mathbb{N}^M \\ u+h=m}} H_{n-e_j,h} X_{u,\kappa}^j\right) - \sum_{n \in \mathbb{N}^N} g_{n,\kappa} H_{n,m}, \quad (A38)$$

$$V_{m,\kappa} := \sum_{j=1}^{M} \sum_{\substack{u,k \in \mathbb{N}^M \\ u+k-e_j=m \\ |k|<m}} w_u u_j S_{k,\kappa}^j + x_{k,\kappa} k_j R_u^j. \quad (A39)$$

Analogous to the autonomous case [see Eq. (A29)], an explicit relation between displacement and velocity parametrization can be established from the invariance equation (A36) as

$$\dot{x}_{m,\kappa} = \Lambda_{m,\kappa} x_{m,\kappa} + \sum_{j=1}^{M} \phi_j S_{m,\kappa}^j + V_{m,\kappa}, \quad (A40)$$

which is identical to the general result of Lemma 4, as we show later. We utilize relation (A40) to rewrite $Y_{m,\kappa}$ in terms of the displacement parametrization and substitute the resulting expression into

the first set of equations in system (A36) to obtain

$$\overbrace{\left(K + \Lambda_{m,\kappa} C + (\Lambda_{m,\kappa})^2 M\right)}^{L_{m,\kappa}} x_{m,\kappa} = D_{m,\kappa} S_{m,\kappa} + C_{m,\kappa}, \quad \text{(A41)}$$

where $C_{m,\kappa} = -\Lambda_{m,\kappa} M V_{m,\kappa} - Y_{m,\kappa}$ and $D_{m,\kappa} \in \mathbb{C}^{n \times M}$ is a matrix whose jth column is given by $(D_{m,\kappa})_j := -(C + M(\lambda_j + \Lambda_{m,\kappa}))\phi_j$ for every $j = 1, \ldots, M$. This concludes the proof of Lemma 3.

For proving Lemma 4, we use the chain rule using the fact that the non-autonomous reduced dynamics trajectories satisfy $\dot{p} = R_\varepsilon(p, \phi)$. To obtain an expression for $\dot{x}$, we collect $\mathcal{O}(\varepsilon)$ terms in the time derivative of the displacement parametrization of the SSM as

$$\dot{x}(p, \phi) = \frac{dw_\varepsilon}{dt}\bigg|_\varepsilon = Dw(p) \cdot S + D_p x \cdot R + D_\phi x \cdot \Omega. \quad \text{(A42)}$$

Finally, we restrict this expression to the multi-index m and harmonic κ to obtain

$$\dot{x}_{m,\kappa} = \sum_{j=1}^{M} \sum_{\substack{u,k \in \mathbb{N}^M \\ u+k-e_j=m}} \left(w_u u_j S_{k,\kappa}^j + x_{k,\kappa} k_j R_u^j\right) + i\langle \Omega, \kappa \rangle x_{m,\kappa}. \quad \text{(A43)}$$

Indeed, the expression in Eq. (A43) is identical to the one based on invariance equation computation given in (A40).

a. Nonautonomous reduced dynamics. Similar to the autonomous case, the underdeterminacy of the linear system (A41) allows for different solution choices for the reduced dynamics parametrization. Specifically, a normal-form style parametrization is appealing when (near-)resonances are present among the master subspace eigenvalues and a given harmonic of the forcing frequency. Indeed, for an eigenvalue λ_i associated with the master subspace, a near-resonance of the form

$$\lambda_i \approx \Lambda_{m,\kappa} \quad \text{(A44)}$$

results in the coefficient matrix $L_{m,\kappa}$ being nearly singular. To ensure (robust) solvability of system (A41), the coefficients $S_{m,\kappa}$ must be chosen such that the right-hand side of system (A41) is orthogonal to the (near) kernel of $L_{m,\kappa}$. In particular, we require (cf. Jain and Haller[34])

$$(\theta_i)^*\left(K + \Lambda_{m,\kappa} C + (\Lambda_{m,\kappa})^2 M\right)x_{m,\kappa} = 0, \quad \text{(A45)}$$

which directly provides the essentially non-zero reduced dynamics coefficients $S_{m,\kappa}^i$ in the normal-form parametrization style as

$$(\theta_i)^*(C + M(\lambda_i + \Lambda_{m,\kappa}))\phi_i S_{m,\kappa}^i$$
$$= -(\theta_i)^*(\Lambda_{m,\kappa} M V_{m,\kappa} + Y_{m,\kappa}). \quad \text{(A46)}$$

3. First-order computation

For general first-order dynamical systems, the equations do not exhibit the internal structure (19) seen for second-order mechanical systems (Lemmas 2 and 4). Hence, we develop general expressions for SSM computation in the first-order system (3). Once again, we operate in physical coordinates using the multi-index notation.

a. Autonomous SSM

We substitute the autonomous first-order SSM expansion

$$W(p) = \sum_{m \in \mathbb{N}^M} W_m p^m, \quad \text{(A47)}$$

where $W_m \in \mathbb{C}^N$, and its reduced dynamics expansion (26) into the autonomous invariance equation (23) to obtain

$$B(\mathrm{D}_p \sum_{u \in \mathbb{N}^M} W_u p^u) \sum_{k \in \mathbb{N}^M} R_k p^k$$
$$= A \sum_{m \in \mathbb{N}^M} W_m p^m + \sum_{n \in \mathbb{N}^N} F_n \left(\sum_{u \in \mathbb{N}^M} W_u p^u\right)^n, \quad \text{(A48)}$$

where $F_n \in \mathbb{R}^N$ are the coefficients in the nonlinearity expansion (A16) in the first-order form. Collecting coefficients of every unique monomial in system (A48), we obtain a linear system for each monomial multi-index m, as we detail below. At the leading order, i.e, for monomial multi-index p^{e_i}, we obtain

$$B\left(\sum_{j=1}^{M} W_{e_j}\right) R_{e_i} = A W_{e_i}. \quad \text{(A49)}$$

From the eigenvalue problem (7), we see that the choice $W_{e_i} = v_i$ and $R_{e_j}^j = \delta_{ij}\lambda_i$ solves Eq. (A49). It is noteworthy that due to this diagonal choice of the leading-order autonomous reduced dynamics, Eq. (A48) get decoupled between distinct multi-indices at each order. Hence, collecting the coefficients of higher-order terms in system (A48) for a multi-index m, we obtain

$$\underbrace{\left(A - \Lambda_m B\right)}_{:=\mathcal{L}_m} W_m = \sum_{j=1}^{M} B v_j R_m^j + \mathcal{C}_m, \quad \text{(A50)}$$

where we define

$$\mathcal{C}_m := \sum_{j=1}^{M} \sum_{\substack{u,k \in \mathbb{N}^M \\ u+k-e_j=m \\ 1<|u|<m}} B W_u u_j R_k^j - \sum_{n \in \mathbb{N}^N} F_n H_{n,m}. \quad \text{(A51)}$$

a. Autonomous reduced dynamics. Analogous to the discussion for second-order systems, we observe that linear system (A50) is underdetermined, which allows for choices of parametrizations for the reduced dynamics. Indeed, for an eigenvalue λ_i associated with the master subspace, a near-resonance of the form (A33) results in the coefficient matrix $\mathcal{L}_m$ being nearly singular. To ensure the solvability of the system (A50), we require (cf. Jain and Haller[34])

$$(u_i)^*\mathcal{L}_m W_m = 0, \quad \text{(A52)}$$

which provides the nonzero reduced dynamics coefficients R_m^i in the normal-form parametrization style as

$$R_m^i = -(u_i)^*\mathcal{C}_m, \quad \text{(A53)}$$

where we have chosen a normalization for the eigenvectors that satisfies $(\boldsymbol{u}_i)^* \boldsymbol{B} \boldsymbol{v}_j = \delta_{ij}$ for every $i, j = 1, \dots, M$.

b. Non-autonomous SSM

To derive the non-autonomous invariance equation in first-order form, we expand the $\mathcal{O}(\varepsilon)$-terms in the non-autonomous SSM

parametrization (20) as

$$\boldsymbol{X}(\boldsymbol{p}, \boldsymbol{\phi}) = \sum_{\boldsymbol{m} \in \mathbb{N}^M} \sum_{\boldsymbol{\kappa} \in \mathbb{Z}^k} \boldsymbol{X}_{\boldsymbol{m},\boldsymbol{\kappa}} e^{i\langle \boldsymbol{\kappa}, \boldsymbol{\phi}\rangle} \boldsymbol{p}^{\boldsymbol{m}}, \qquad (A54)$$

where $\boldsymbol{X}_{\boldsymbol{m},\boldsymbol{\kappa}} \in \mathbb{C}^N$. Substituting the expansions (A54) and (34) into the nonautonomous invariance equation (31), and collecting terms corresponding to any given Fourier-harmonic $\boldsymbol{\kappa}$, we obtain

$$\boldsymbol{B} \left(D_{\boldsymbol{p}} \left(\sum_{\boldsymbol{u} \in \mathbb{N}^M} \boldsymbol{W}_{\boldsymbol{u}} \boldsymbol{p}^{\boldsymbol{u}} \right) \sum_{\boldsymbol{k} \in \mathbb{N}^M} \boldsymbol{S}_{\boldsymbol{k},\boldsymbol{\kappa}} \boldsymbol{p}^{\boldsymbol{k}} + \left(\partial_{\boldsymbol{p}} \sum_{\boldsymbol{u} \in \mathbb{N}^M} \boldsymbol{X}_{\boldsymbol{u},\boldsymbol{\kappa}} \boldsymbol{p}^{\boldsymbol{u}} \right) \sum_{\boldsymbol{k} \in \mathbb{N}^M} \boldsymbol{R}_{\boldsymbol{k}} \boldsymbol{p}^{\boldsymbol{k}} + i\langle \boldsymbol{\kappa}, \boldsymbol{\Omega} \rangle \sum_{\boldsymbol{m} \in \mathbb{N}^M} \boldsymbol{X}_{\boldsymbol{m},\boldsymbol{\kappa}} \boldsymbol{p}^{\boldsymbol{m}} \right)$$

$$= \boldsymbol{A} \sum_{\boldsymbol{m} \in \mathbb{N}^M} \boldsymbol{X}_{\boldsymbol{m},\boldsymbol{\kappa}} \boldsymbol{p}^{\boldsymbol{m}} + \left[D_{\boldsymbol{z}} \boldsymbol{F}_n \left(\sum_{\boldsymbol{u} \in \mathbb{N}^M} \boldsymbol{W}_{\boldsymbol{u}} \boldsymbol{p}^{\boldsymbol{u}} \right)^n \right] \sum_{\boldsymbol{m} \in \mathbb{N}^M} \boldsymbol{X}_{\boldsymbol{m},\boldsymbol{\kappa}} \boldsymbol{p}^{\boldsymbol{m}} + \sum_{\boldsymbol{n} \in \mathbb{N}^N} \sum_{\boldsymbol{m} \in \mathbb{N}^M} \boldsymbol{G}_{\boldsymbol{n},\boldsymbol{\kappa}} H_{\boldsymbol{n},\boldsymbol{m}}, \qquad (A55)$$

where $\boldsymbol{G}_{\boldsymbol{n},\boldsymbol{\kappa}} \in \mathbb{C}^N$ are the coefficients in the forcing expansion (A17) in the first-order form. Finally, collecting the coefficients corresponding to any given monomial multi-index $\boldsymbol{m}$ in system (A55), we obtain (cf. Ponsioen *et al.*[60])

$$\underbrace{\left(\boldsymbol{A} - (\boldsymbol{\Lambda}_{\boldsymbol{m}} + i\langle \boldsymbol{\kappa}, \boldsymbol{\Omega} \rangle) \boldsymbol{B} \right)}_{:= \mathcal{L}_{\boldsymbol{m},\boldsymbol{\kappa}}} \boldsymbol{X}_{\boldsymbol{m},\boldsymbol{\kappa}} = \sum_{j=1}^{M} \boldsymbol{B} \boldsymbol{v}_j S^j_{\boldsymbol{m},\boldsymbol{\kappa}} + \mathcal{C}_{\boldsymbol{m},\boldsymbol{\kappa}}, \qquad (A56)$$

where

$$\mathcal{C}_{\boldsymbol{m},\boldsymbol{\kappa}} := \boldsymbol{B} \left(\sum_{j=1}^{M} \sum_{\substack{\boldsymbol{u},\boldsymbol{k} \in \mathbb{N}^M \\ \boldsymbol{u}+\boldsymbol{k}-\boldsymbol{e}_j = \boldsymbol{m} \\ |\boldsymbol{k}| < m}} \boldsymbol{W}_{\boldsymbol{u}} u_j S^j_{\boldsymbol{k},\boldsymbol{\kappa}} \sum_{j=1}^{M} \sum_{\substack{\boldsymbol{u},\boldsymbol{k} \in \mathbb{N}^M \\ \boldsymbol{u}+\boldsymbol{k}-\boldsymbol{e}_j = \boldsymbol{m} \\ |\boldsymbol{u}| < m}} \boldsymbol{X}_{\boldsymbol{u},\boldsymbol{\kappa}} u_j R^j_{\boldsymbol{k}} \right)$$

$$- \sum_{\boldsymbol{n} \in \mathbb{N}^N} \boldsymbol{G}_{\boldsymbol{n},\boldsymbol{\kappa}} H_{\boldsymbol{n},\boldsymbol{m}} - \sum_{\boldsymbol{n} \in \mathbb{N}^N} \boldsymbol{F}_n \sum_{j=1}^{2n} n_j \left(\sum_{\substack{\boldsymbol{u},\boldsymbol{h} \in \mathbb{N}^M \\ \boldsymbol{u}+\boldsymbol{h}=\boldsymbol{m}}} H_{\boldsymbol{n}-\boldsymbol{e}_j,\boldsymbol{h}} X^j_{\boldsymbol{u},\boldsymbol{\kappa}} \right). \qquad (A57)$$

Recursively solving the linear system (A56) provides us the coefficients $\boldsymbol{X}_{\boldsymbol{m},\boldsymbol{\kappa}}, \boldsymbol{S}_{\boldsymbol{m},\boldsymbol{\kappa}}$ defining the $\mathcal{O}(\varepsilon)$-terms in the parametrizations for the nonautonomous SSM and its reduced dynamics. At the leading order, system (A56) simplifies as (cf. Jain and Haller[34])

$$\left(\boldsymbol{A} - i\langle \boldsymbol{\kappa}, \boldsymbol{\Omega} \rangle \boldsymbol{B} \right) \boldsymbol{X}_{0,\boldsymbol{\kappa}} = \sum_{j=1}^{M} \boldsymbol{B} \boldsymbol{v}_j S^j_{0,\boldsymbol{\kappa}} + \boldsymbol{G}_{0,\boldsymbol{\kappa}}. \qquad (A58)$$

At any higher order $m = |\boldsymbol{m}| > 1$, we have $z_m = \binom{m+M-1}{M-1}$ distinct multi-indices. An important consequence of choosing the linear autonomous reduced dynamics to be diagonal, i.e., $R^i_{\boldsymbol{e}_j} = \delta_{ij} \lambda_j$, is that the system (A56) gets decoupled between distinct multi-indices at any given order m and for any given harmonic $\boldsymbol{\kappa}$. Thus, instead of

solving $z_m \times N$ coupled linear equations in general, we need to solve only z_m linear systems of dimension N each.

a. Reduced dynamics. Analogous to the discussion for second-order nonautonomous setting, we observe that the linear system (A56) is underdetermined, which allows for choices of parametrizations for the reduced dynamics. Indeed, for an eigenvalue λ_i associated with the master subspace, a near-resonance of the form (36) results in the coefficient matrix $\mathcal{L}_{\boldsymbol{m},\boldsymbol{\kappa}}$ being nearly singular.

To ensure (robust) solvability of system (A56), the coefficients $\boldsymbol{S}_{\boldsymbol{m},\boldsymbol{\kappa}}$ must be chosen such that the right-hand side of system (A41) is orthogonal to the (near) kernel of $\mathcal{L}_{\boldsymbol{m},\boldsymbol{\kappa}}$. In particular, we require

$$(\boldsymbol{u}_i)^* \mathcal{L}_{\boldsymbol{m},\boldsymbol{\kappa}} \boldsymbol{X}_{\boldsymbol{m},\boldsymbol{\kappa}} = 0, \qquad (A59)$$

which directly provides us the essentially non-zero reduced dynamics coefficients $S^i_{\boldsymbol{m},\boldsymbol{\kappa}}$ in the normal-form parametrization style as

$$S^i_{\boldsymbol{m},\boldsymbol{\kappa}} = (\boldsymbol{u}_i)^* \mathcal{C}_{\boldsymbol{m},\boldsymbol{\kappa}}. \qquad (A60)$$

Specifically, at the leading order, we have $S^i_{0,\boldsymbol{\kappa}} = (\boldsymbol{u}_i)^* \boldsymbol{G}_{0,\boldsymbol{\kappa}}$ (cf. Jain and Haller[34]).

APPENDIX B: PROOF OF LEMMA 5

In this section, we provide the proofs for the statements in Lemma 5. We use a polar transformation of the parametrization coordinates $\boldsymbol{p} = [p, \overline{p}] = [\rho e^{i\theta}, \rho e^{-i\theta}]$. Thus, $\dot{p} = (\dot{\rho} + \rho i\dot{\theta})e^{i\theta}$. Specifically, the reduced dynamics (40) over the two-dimensional

nonautonomous SSM ($M = 2$) transforms as

$$(\dot{\rho} + \rho i \dot{\theta}) = \sum_{\boldsymbol{m} \in \mathbb{N}^l} R_{\boldsymbol{m}}^1 (\rho e^{i\theta})^{m_1} (\rho e^{-i\theta})^{m_2} e^{-i\theta}$$

$$+ \varepsilon \sum_{\substack{\boldsymbol{m} \in \mathbb{N}^l \\ \kappa \in \mathbb{Z}}} S_{\boldsymbol{m},\kappa}^1 e^{i\kappa\phi} (\rho e^{i\theta})^{m_1} (\rho e^{-i\theta})^{m_2} e^{-i\theta} \quad \text{(B1)}$$

$$= \sum_{\boldsymbol{m} \in \mathbb{N}^l} R_{\boldsymbol{m}}^1 \rho^{|\boldsymbol{m}|} e^{i\theta(m_1 - m_2 - 1)}$$

$$+ \varepsilon \sum_{\substack{\boldsymbol{m} \in \mathbb{N}^l \\ \kappa \in \mathbb{Z}^*}} S_{\boldsymbol{m},\kappa}^1 \rho^{|\boldsymbol{m}|} e^{i\kappa\phi} e^{i\theta(m_1 - m_2 - 1)}. \quad \text{(B2)}$$

Choosing a normal-form style of parametrization (A35) for the autonomous reduced dynamics, we obtain nonzero coefficients $R_{\boldsymbol{m}}^1$ only for multi-indices that satisfy the near resonance condition (28). Hence, we have $m_1 - m_2 - 1 = 0$ for every nonzero $R_{\boldsymbol{m}}^1$. Thus, the angular part vanishes for all autonomous terms in Eq. (B2).

Furthermore, choosing a normal-form style of parametrization (A46) for the nonautonomous reduced dynamics, we obtain nonzero coefficients $S_{\boldsymbol{m},\kappa}^1$ only for the pairs $(\boldsymbol{m},\kappa)$ that satisfy the near-resonance condition (36). But under the external near-resonance condition (54), for any pair $(\boldsymbol{m},\kappa)$ that fulfills the near-resonance conditions (36), we have $\kappa = (1 - m_1 + m_2)\kappa_0$. This allows us to rewrite $e^{i\kappa\phi} e^{i\theta(m_1 - m_2 - 1)} = e^{i(\kappa/\kappa_0)(\kappa_0\phi - \theta)}$ in Eq. (B2). Now, introducing the phase shift $\psi = \theta - \kappa_0\phi$ in Eq. (B2) and using the fact that $\dot{\phi} = \Omega$, we obtain

$$(\dot{\rho} + \rho i (\dot{\psi} + \kappa_0 \Omega)) = \sum_{\boldsymbol{m} \in \mathbb{N}^l} R_{\boldsymbol{m}}^1 \rho^{|\boldsymbol{m}|}$$

$$+ \varepsilon S_{\boldsymbol{0},\kappa_0}^1 e^{-i\psi} + \varepsilon \sum_{\substack{\boldsymbol{m} \in \mathbb{N}^l \\ \kappa \in \mathbb{Z}^*}} S_{\boldsymbol{m},\kappa}^1 e^{-i(\kappa/\kappa_0)\psi}. \quad \text{(B3)}$$

Finally, separating the real and imaginary parts of Eq. (B3) results in Eq. (55), which concludes the proof of statement (i). The zeros of the function

$$\boldsymbol{r}(\rho, \psi, \Omega) = \boldsymbol{0} \quad \text{(B4)}$$

correspond to fixed points of the polar dynamics (55). For the original non-autonomous reduced dynamics (40), such a fixed point represents a trajectory with a constant phase shift ψ relative to the forcing as well as a constant polar amplitude ρ. Hence, this fixed point describes a periodic orbit of the reduced dynamics. As the SSM parametrization maps the orbits of the reduced system onto the orbits of the full system, we obtain a periodic steady state for the full system, which concludes the proof of statement (ii). For computing the stability of these fixed points, we rewrite the polar dynamics (B3) in the form

$$\begin{bmatrix} \dot{\rho} \\ \dot{\psi} \end{bmatrix} = \begin{bmatrix} a(\rho) \\ b(\rho)/\rho \end{bmatrix} + \varepsilon \left(\frac{\boldsymbol{N}(\psi)}{\rho} \begin{bmatrix} \text{Re } (S_{\boldsymbol{0},\kappa_0}^1) \\ \text{Im } (S_{\boldsymbol{0},\kappa_0}^1) \end{bmatrix} \right.$$

$$\left. + \sum_{\substack{\boldsymbol{m} \in \mathbb{N}^2 \\ \kappa \in \mathbb{Z}}} \rho^{|\boldsymbol{m}|-1} \boldsymbol{N}((\kappa/\kappa_0)\psi) \begin{bmatrix} \text{Re } (S_{\boldsymbol{m},\kappa}^1) \\ \text{Im } (S_{\boldsymbol{m},\kappa}^1) \end{bmatrix} \right). \quad \text{(B5)}$$

Evaluating the Jacobian of the right-hand side of Eq. (B5) at a hyperbolic fixed point (ρ, ψ) concludes its stability via linearization. This proves statement (iii).

APPENDIX C: DETAILS ON THE CONTINUATION ROUTINE

Within `SSMTool 2.4` as well as for the full-system analysis, we make use of the `po` toolbox provided by the continuation toolbox `COCO`.[28] In this section, we give details on performing parameter continuation over the SSM-based ROMs. We also list the continuation parameters used for each example in this paper.

1. Sensitivity coefficients

For an efficient numerical continuation of periodic orbits in `COCO`, the Jacobian of the reduced vector field with respect to the continuation parameters ε and Ω and with respect to the parametrization coordinates $\boldsymbol{p}$ should be provided. The Jacobian with respect to the parametrization coordinates is straightforward, as the vector field is polynomial in $\boldsymbol{p}$. For the derivative with respect to the forcing amplitude ε, only the $\mathcal{O}(\varepsilon)$ terms need to be considered, which yields

$$\partial_\varepsilon \boldsymbol{R}_\varepsilon(\boldsymbol{p}, \phi) = \boldsymbol{S}(\boldsymbol{p}, \phi). \quad \text{(C1)}$$

As the nonautonomous coefficients are obtained by solving system (35), they implicitly depend on the forcing frequency, i.e., $\boldsymbol{S}_{\boldsymbol{m},\kappa} = \boldsymbol{S}_{\boldsymbol{m},\kappa}(\Omega)$. Accounting for this frequency dependence of the reduced dynamics coefficients, we write the derivative with respect to Ω as

$$\partial_\Omega \boldsymbol{R}_\varepsilon(\boldsymbol{p}, \boldsymbol{\phi}) = \varepsilon \sum_{\boldsymbol{m} \in \mathbb{N}^M} \sum_{\kappa \in \mathbb{Z}} (\partial_\Omega \boldsymbol{S}_{\boldsymbol{m},\kappa} e^{i\kappa\Omega t} + i\kappa t \boldsymbol{S}_{\boldsymbol{m},\kappa} e^{i\kappa\Omega t}) \boldsymbol{p}^{\boldsymbol{m}}, \quad \text{(C2)}$$

The sensitivity coefficients $\partial_\Omega \boldsymbol{S}_{\boldsymbol{m},\kappa}$ can be computed by taking the derivative of Eq. (A60) with respect to Ω. Alternatively, one may choose to ignore these coefficients in Eq. (C2). This second choice may lead to an inaccurate computation of the Jacobian, which may reduce the rate of convergence to the solution during numerical continuation. However, it does not compromise the solution accuracy, which is controlled by separate numerical tolerances (see Table VIII). These tolerances are related to the solution of the invariance equations and to the residual in the Newton iteration, which we evaluate up to machine precision. Opreni et al.[61] extend this choice to the SSM and its reduced dynamics parametrizations by assuming the coefficients $\boldsymbol{X}_{\boldsymbol{m},\kappa}, \boldsymbol{S}_{\boldsymbol{m},\kappa}$ to be independent of the forcing frequency Ω and computing them only once across the entire frequency range. Such an assumption cannot guarantee solution accuracy, but offers additional computational advantages. Hence, in contrast to Opreni et al.,[61] we choose to solve the nonautonomous invariance equations for each value of the forcing frequency here.

2. Period-doubling bifurcations and stability boundary

The `po`-toolbox of `COCO`, which is used for periodic-orbit continuation in our SSM-based ROMs as well as in the full system, uses Floquet multipliers to determine the stability of a periodic orbit

and detect bifurcations (if any). Specifically, a change in the stability of a periodic orbit occurs when a Floquet multiplier crosses the unit circle in the complex plane, resulting in a period-doubling bifurcation.[28,55] In a system subject to periodic, parametric excitation, switching to a branch of period-doubling bifurcations and performing continuation along this branch using COCO then provides us the stability boundary for the trivial periodic response.

3. Details on computational complexity

In Tables VI and VII, we enlist the basic steps and associated computational complexity associated with SSM-ROM

and full-system collocation (see Secs. V B and VI B for details).

4. Parameters for collocation

The parameters for the continuation of the SSM-based ROMs are presented in Table IX. Table X lists the collocation and continuation parameters used for various simulations of the full system. Note that since the level set method of SSMTool 2.4 does not require continuation and relies solely on the evaluation of the zero level set of a function, there are no continuation parameters listed

TABLE VI. Basic steps and the associated computational complexity to obtain a stability diagram/FRC via SSM-based ROM and via full-system collocation (see Sec. V B). The general symbols i, n_c, and c denote the number of linear system solves required for an iterative solution of a nonlinear algebraic system, the number of continuation steps, and the number of collocation points used to approximate a periodic solution.

Steps		SSM-ROM	Full-system collocation
1. Master subspace			
i	Complexity of solving eigenvalue problem	$\mathcal{O}(n^3)$	...
2. Autonomous SSM			
ii	Linear system dimension	n	...
iii	Number of linear system solves	Σ_Γ	...
iv	Computational complexity	$\Sigma_\Gamma \cdot \mathcal{O}(n^3)$	...
v	Parallelizability over monomials (m)	Yes	...
vi	Parallelized complexity	$\Gamma \cdot \mathcal{O}(n^3)$	...
3. Nonautonomous SSM			
vii	Linear system dimension	n	...
viii	Number of linear system solves	$\Sigma_{\Gamma,h}$	...
ix	Computational complexity	$\Sigma_{\Gamma,h} \cdot \mathcal{O}(n^3)$	...
x	Parallelizability over monomials (m)	Yes	...
xi	Parallelizability over harmonics (κ)	Yes	...
xii	Parallelized complexity	$\Gamma h \cdot \mathcal{O}(n^3)$	...
4. Collocation-based numerical continuation			
xiii	Nonlinear algebraic system dimension	$2c$	$2nc$
xiv	Number of iterations (linear system solves per continuation step)	i	i
xv	Computational complexity	$i \cdot \mathcal{O}(c^3)$	$i \cdot \mathcal{O}((nc)^3)$
xvi	Number of continuation steps	n_c	n_c
	Overall computational complexity (i + iv +xvi [ix + xv])	$\mathcal{O}(n^3) + \Sigma_\Gamma \cdot \mathcal{O}(n^3) + n_c\left[\Sigma_{\Gamma,h} \cdot \mathcal{O}(n^3) + i \cdot \mathcal{O}(c^3)\right]$	$n_c i \cdot \mathcal{O}((nc)^3)$
	Overall parallelized complexity (i + vi +xvi [xii + xv])	$\mathcal{O}(n^3) + \Gamma \cdot \mathcal{O}(n^3) + n_c\left[\Gamma h \cdot \mathcal{O}(n^3) + i \cdot \mathcal{O}(c^3)\right]$	...

TABLE VII. Basic steps and the associated computational complexity to obtain an FRC via Lemma 5 (SSM) and via full-system collocation (see Sec. VI B). The preceding steps for SSM reduction are the same as steps 1-3 given in Table VI. For the SSM routine, the frequencies at which the periodic orbits are computed can be set explicitly, and the total number of solutions is denoted by n_Ω. For the continuation routine, in contrast, a frequency interval is provided, along which a family of solutions is computed using n_c steps.

Steps		SSM-ROM	Full-system collocation
4. FRC computation			
xiii	Nonlinear algebraic system dimension	2	$2nc$
xiv	Number of iterations per (continuation/frequency) step	−	i
xv	Computational complexity	$\mathcal{O}(1)$	$i \cdot \mathcal{O}(n^3 c^3)$
xvi	Number of steps	n_Ω	n_c
xvii	Parallelizability over Ω	Yes	No
	Overall computational complexity (i + iv +xvi [ix + xv])	$\mathcal{O}(n^3) + \Sigma_\Gamma \cdot \mathcal{O}(n^3) + n_\Omega\left[(\Sigma_{\Gamma,h} \cdot \mathcal{O}(n^3)\right]$	$n_c i \cdot \mathcal{O}((nc)^3)$
	Overall parallelized complexity (i + vi +xii + xv)	$\mathcal{O}(n^3) + \Gamma \cdot \mathcal{O}(n^3) + \Gamma h \cdot \mathcal{O}(n^3)$	...

TABLE VIII. Parameters for continuation with po.[28]

Parameter	Default	Description
NAdapt	0	Period for refinement of coll. mesh
h_0	0.1	Initial continuation stepsize
h_max	0.5	Max. continuation stepsize
h_min	0.01	Min. continuation stepsize
h_fac_max	2	Max. factor for adapting stepsize
h_fac_min	0.5	Min. factor for adapting stepsize
MaxRes	0.1	Maximal residual norm
bi_direct	1	Bidirectional continuation (boolean)
PtMX	100	Max. number of continuation steps
al_max	7	Max. angle btw. consecutive tangents
ItMX	10	Iterations before adapting stepsize
TOL	1×10^{-6}	Tolerance for Newton Iteration
NTST	10	Sub-intervals in coll. discretization
NCOL	4	Number of collocation points

for the examples in Sec. VI C. Table VIII gives a short description of each parameter along with its default value in COCO.

APPENDIX D: MODAL EQUATIONS FOR THE PRISMATIC BEAM

In this section, we derive the ODEs governing the evolution of the modal coordinates of a clamped-hinged prismatic beam as a function of the physical parameters, i.e., elastic modulus E, density ρ, radius of gyration r, area A, and moment of inertia of the cross section I, and a characteristic length L. The characteristic length may be the length of the beam or a typical wavelength for oscillatory modes of the beam. We generally assume that the beam length is obtained by multiplying the characteristic length L by a dimensionless constant l as lL. At the hinged end, the beam is subject to an axial load $p_a(t)$. The PDE governing the behavior of the transverse displacement w of the beam in a nondimensional form is given as[67,68]

$$\frac{\partial^4 w}{\partial y^4} + \frac{\partial^2 w}{\partial t^2} = \delta \left(H \frac{\partial^2 w}{\partial y^2} - 2c \frac{\partial w}{\partial t} - p_a(t) \frac{\partial^2 w}{\partial y^2} \right), \quad \text{(D1)}$$

$$w(0) = w''(0) = w(l) = w'(l) = 0, \quad \text{(D2)}$$

TABLE IX. Collocation and continuation parameters set in the po-toolbox of coco for the SSM-based ROMs in different examples.

Figure Parameter	3(a) Value	3(b)	5(a)	5(b)	6	7
NAdapt	0	0	0	0	0	1
h_0	0.1	1×10^{-4}	0.1	1×10^{-4}	0.1	1×10^{-4}
h_max	0.5	0.5	0.5	0.5	0.5	50
h_min	0.01	1×10^{-4}	0.01	1×10^{-4}	0.01	1×10^{-4}
bi_direct	1	0	1	0	1	0
PtMX	50	35	50	40	50	60

where the following dimensionless quantities are used:[67]

$$y = \frac{y'}{L}, \quad t = \sqrt{\frac{Er^2}{\rho L^4}} t', \quad \text{(D3)}$$

$$w = \frac{L}{r^2} w', \quad c = \frac{L^4}{2r^3 \sqrt{\rho E}} \frac{r^2}{L^2} c', \quad \text{(D4)}$$

with $(\bullet)'$ denoting the corresponding quantities in physical units. Specifically, c' is the distributed damping coefficient; y', t', w' represent the axial coordinate, the time, and the transverse displacement. The axial stretching forces due to the nonlinear bending-stretching coupling are accounted by the term H defined as

$$H = \frac{1}{2l} \int_0^l \left(\frac{\partial w}{\partial y} \right)^2 \, dy. \quad \text{(D5)}$$

In this example, we choose the slenderness ratio $\delta := \frac{r^2}{L^2}$ to be 10^{-4} in line with the original treatment of Nayfeh *et al.*,[67] who analyze the prismatic beam under weak nonlinearities. A modal expansion of the displacement field w yields

$$w(y, t) = \sum_i \psi_i(y) z_i(t), \quad \text{(D6)}$$

where $\psi_i(y)$ denotes the ith eigenfunction associated with the eigenfrequency ω_i of the linearized version of the PDE (D1) around the trivial solution. These eigenfunctions are solutions of the eigenvalue

TABLE X. Collocation and continuation parameters set in the po-toolbox of coco for the full system in different examples.

Figure Parameter	3(a) Value	3(b)	5(a)	5(b)	6	7	9	10	10 Isola
NAdapt	0	0	0	1	0	1	1	1	1
h_0	0.1	1×10^{-4}	0.1	0.1	0.1	1×10^{-4}	0.1	0.1	0.1
h_max	0.5	0.5	0.5	0.5	0.5	50	0.5	0.5	0.5
MaxRes	0.1	0.1	0.1	0.1	0.1	0.1	0.1	0.1	0.1
bi_direct	1	0	1	0	1	0	1	1	0
PtMX	10	60	100	60	100	500	350	200	90
ItMX	10	15	10	15	10	15	10	10	10
NTST	10	30	10	10	10	70	70	20	80

problem,

$$\frac{\partial^4 \psi_i}{\partial y^4} = \omega_i^2 \psi_i, \tag{D7}$$

$$\psi(0) = \psi''(0) = \psi(l) = \psi'(l) = 0, \tag{D8}$$

where we choose an orthonormal representation for these eigenfunctions, i.e.,

$$\int_0^l \psi_i(y)\psi_j(y)\mathrm{d}y = \delta_{ij}. \tag{D9}$$

Nayfeh *et al.*[67] have computed explicit expressions for these eigenfunctions in terms of trigonometric and hyperbolic functions. Substituting the modal expansion (D6) into system (D1), and performing a Galerkin projection, we obtain the set of ODEs governing the evolution of the modal coordinates $z_j(t)$ as

$$\omega_j^2 z_j + \ddot{z}_j + 2c\delta\dot{z}_j = \sum_{i,k,s} \delta\alpha_{jiks}z_iz_kz_s + \delta \sum_i p_a(t)z_ia_{ji}, \tag{D10}$$

where

$$a_{ji} = \int_0^l \psi_j \, \psi_i'' \mathrm{d}y, \tag{D11}$$

$$\alpha_{jiks} = \left(\int_0^l \psi_s' \psi_k' \mathrm{d}y\right)\left(\int_0^l \psi_j \psi_i'' \mathrm{d}y\right). \tag{D12}$$

We have assumed the external load to be applied at the hinged tip of the beam and set the transversal excitation to zero. Hence, the axial forcing effectively leads to a parametric excitation of the transverse modal coordinates in system (D10).

REFERENCES

[1] A. Champneys, "Dynamics of parametric excitation," in *Encyclopedia of Complexity and Systems Science* (Springer, New York, 2013), see https://doi.org/10.1007/978-3-642-27737-5_144-3.

[2] L. Sanches, G. Michon, A. Berlioz, and D. Alazard, "Parametrically excited helicopter ground resonance dynamics with high blade asymmetries," J. Sound Vib. **331**, 3897–3913 (2012).

[3] R. P. Coleman and A. M. Feingold, see https://digital.library.unt.edu/ark:/67531/metadc60767/m1/3/ for "Theory of Self-Excited Mechanical Oscillations of Helicopter Rotors with Hinged Blades" (1956).

[4] H. Ecker, "Beneficial effects of parametric excitation in rotor systems," in *IUTAM Bookseries* (Springer, Dordrecht, 2011), Vol. 25, pp. 361–371, see https://link.springer.com/chapter/10.1007/978-94-007-0020-8_31.

[5] M. G. Tehrani, E. Bonisoli, and M. Scapolan, "Energy harvesting perspectives from parametric resonant systems," in *Conference Proceedings of the Society for Experimental Mechanics Series* (Springer, Cham, 2015), Vol. 9, pp. 223–232 , see https://link.springer.com/chapter/10.1007/978-3-319-15233-2_23.

[6] J. F. Rhoads *et al.*, "Generalized parametric resonance in electrostatically actuated microelectromechanical oscillators," J. Sound Vib. **296**, 797–829 (2006).

[7] L. Li, T. Hiller, B. Bamieh, and K. Turner, "Amplitude control of parametric resonances for mass sensing," in *Proceedings of IEEE Sensors* (Institute of Electrical and Electronics Engineers Inc., 2014), Vol. 2014, pp. 198–201.

[8] J. Welte, T. J. Kniffka, and H. Ecker, "Parametric excitation in a two degree of freedom MEMS system," Shock Vib. **20**, 1113–1124 (2013).

[9] P. M. Polunin and S. W. Shaw, "Self-induced parametric amplification in ring resonating gyroscopes," Int. J. Non-Linear Mech. **94**, 300–308 (2017).

[10] M. Sharma, E. H. Sarraf, R. Baskaran, and E. Cretu, "Parametric resonance: Amplification and damping in MEMS gyroscopes," Sens. Actuators, A **177**, 79–86 (2012).

[11] A. Frangi, A. Guerrieri, R. Carminati, and G. Mendicino, "Parametric resonance in electrostatically actuated micromirrors," IEEE Trans. Ind. Electron. **64**, 1544–1551 (2017).

[12] J. F. Rhoads and S. W. Shaw, The effects of nonlinearity on parametric amplifiers," in *Proceedings of the ASME Design Engineering Technical Conference* (American Society of Mechanical Engineers Digital Collection, 2009), Vol. 4, pp. 593–597.

[13] F. Verhulst, "Parametric and autoparametric resonance," Acta Appl. Math. **70**, 231–264 (2002).

[14] F. Verhulst, see https://link.springer.com/referenceworkentry/10.1007/978-0-387-30440-3_393 for "Perturbation Analysis of Parametric Resonance" (2009).

[15] Y. Jia, S. Du, and A. A. Seshia, "Twenty-eight orders of parametric resonance in a microelectromechanical device for multi-band vibration energy harvesting," Sci. Rep. **6**, 1–8 (2016).

[16] A. A. Grandi, S. Protière, and A. Lazarus, "Enhancing and controlling parametric instabilities in mechanical systems," Extreme Mech. Lett. **43**, 101195 (2021).

[17] F. Verhulst, *Nonlinear Differential Equations and Dynamical Systems* (Springer, Berlin, 1996).

[18] J. Warminski, "Regular and chaotic vibrations of a parametrically and self-excited system under internal resonance condition," Meccanica **40**, 181–202 (2005).

[19] J. F. Rhoads, S. W. Shaw, and K. L. Turner, "The nonlinear response of resonant microbeam systems with purely parametric electrostatic actuation," J. Micromech. Microeng. **16**, 890 (2006).

[20] D. Li and S. W. Shaw, "The effects of nonlinear damping on degenerate parametric amplification," Nonlinear Dyn. **102**, 2433–2452 (2020).

[21] B. Zaghari, E. Rustighi, and M. G. Tehrani, Dynamic response of a nonlinear parametrically excited system subject to harmonic base excitation," J. Phys.: Conf. Ser. **744**, 012125 (2016).

[22] K. Szabelski and J. Warminski, "Self-excited system vibrations with parametric and external excitations," J. Sound Vib. **187**, 595–607 (1995).

[23] K. Szabelski and J. Warminski, "Vibration of a non-linear self-excited system with two degrees of freedom under external and parametric excitation," Nonlinear Dyn. **14**, 23–36 (1997).

[24] V. S. Sorokin and J. J. Thomsen, "Vibration suppression for strings with distributed loading using spatial cross-section modulation," J. Sound Vib. **335**, 66–77 (2015).

[25] M. Aghamohammadi, V. Sorokin, and B. Mace, "Dynamic analysis of the response of Duffing-type oscillators subject to interacting parametric and external excitations," Nonlinear Dyn. **107**, 99–120 (2022).

[26] J. Warminski and J. M. Balthazar, "Vibrations of a parametrically and self-excited system with ideal and non-ideal energy sources," J. Braz. Soc. Mech. Sci. Eng. **25**, 413–420 (2003).

[27] E. Doedel and B. Oldeman, see http://indy.cs.concordia.ca/auto/ for "AUTO: Software for Continuation and Bifurcation Problems in Ordinary Differential Equations" (2007).

[28] H. Dankowicz and F. Schilder, *Recipes for Continuation* (Society for Industrial and Applied Mathematics, 2013), see https://epubs.siam.org/page/terms.

[29] A. Dhooge, W. Govaerts, Y. A. Kuznetsov, H. G. Meijer, and B. Sautois, "New features of the software matcont for bifurcation analysis of dynamical systems," Math. Comp. Model. Dyn. Syst. **14**, 147–175 (2008).

[30] A. Salinger *et al.*, *Loca 1.1. Library of Continuation Algorithms: Theory and Implementation Manual* (Sandia National Laboratories, Albuquerque, NM, 2002).

[31] S. Karkar *et al.*, see http://manlab.lma.cnrs-mrs.fr/ for "Manlab: An Interactive Path-Following and Bifurcation Analysis Software" (2019).

[32] M. Krack and J. Gross, *Harmonic Balance for Nonlinear Vibration Problems* (Springer International Publishing, 2019).

[33] J. Marconi, P. Tiso, D. E. Quadrelli *et al.* "A higher-order parametric nonlinear reduced-order model for imperfect structures using Neumann expansion," Nonlinear Dyn. **104**, 3039–3063 (2021).

[34]S. Jain and G. Haller, "How to compute invariant manifolds and their reduced dynamics in high-dimensional finite element models," Nonlinear Dyn. **107**, 1417–1459 (2021).

[35]M. Li, S. Jain, and G. Haller, "Nonlinear analysis of forced mechanical systems with internal resonance using spectral submanifolds, part I: Periodic response and forced response curve," Nonlinear Dyn. **110**, 1005–1043 (2022).

[36]A. Opreni, A. Vizzaccaro, A. Frangi, and C. Touzé, "Model order reduction based on direct normal form: Application to large finite element MEMS structures featuring internal resonance," Nonlinear Dyn. **105**, 1237–1272 (2021).

[37]J. Hansen, "Stability diagrams for coupled Mathieu-equations," in *Ingenieur-Archiv* (Springer, 1985), Vol. 55, pp. 463–473, see https://link.springer.com/article/10.1007/BF00537654.

[38]K. G. Lindh and P. W. Likins, "Infinite determinant methods for stability analysis of periodic-coefficient differential equations," AIAA J. **8**, 680–686 (1970).

[39]S. Shaw and C. Pierre, "Non-linear normal modes and invariant manifolds," J. Sound Vib. **150**, 170–173 (1991).

[40]J. Warminski, K. Kecik, A. Mitura, and M. Bochenski, "Nonlinear phenomena in mechanical system dynamics," J. Phys.: Conf. Ser. **382**, 012004 (2012).

[41]S. C. Sinha, S. Redkar, V. Deshmukh, and E. A. Butcher, "Order reduction of parametrically excited nonlinear systems: Techniques and applications," Nonlinear Dyn. **41**, 237–273 (2005).

[42]S. C. Sinha, S. Redkar, and E. A. Butcher, "Order reduction of nonlinear systems with time periodic coefficients using invariant manifolds," J. Sound Vib. **284**, 985–1002 (2005).

[43]S. W. Shaw and C. Pierre, "Normal modes for non-linear vibratory systems," J. Sound Vib. **164**, 85–124 (1993).

[44]G. Haller, B. Kaszás, A. Liu, and J. Axås, "Nonlinear model reduction to fractional and mixed-mode spectral submanifolds," Chaos **33**, 063138 (2023).

[45]X. Cabré, E. Fontich, and R. De la Llave, "The parameterization method for invariant manifolds. I: Manifolds associated to non-resonant subspaces," Indiana Univ. Math. J. **52**, 283–328 (2003).

[46]X. Cabré, E. Fontich, and R. De la Llave, "The parameterization method for invariant manifolds. II: Regularity with respect to parameters," Indiana Univ. Math. J. **52**, 329–360 (2003).

[47]X. Cabré, E. Fontich, and R. de la Llave "The parameterization method for invariant manifolds. III: Overview and applications," J. Differ. Equation **218**(2), 444–515 (2005).

[48]A. Haro, M. Canadell, J.-L. Figueras, A. Luque, and J. M. Mondelo, *The Parameterization Method for Invariant Manifolds*, Applied Mathematical Sciences Vol. 1 (Springer International Publishing, Cham, 2016), see http://link.springer.com/10.1007/978-3-319-29662-3.

[49]G. Haller and S. Ponsioen, "Nonlinear normal modes and spectral submanifolds: Existence, uniqueness and use in model reduction," Nonlinear Dyn. **86**, 1493–1534 (2016).

[50]G. Haller and S. Ponsioen, "Exact model reduction by a slow–fast decomposition of nonlinear mechanical systems," Nonlinear Dyn. **90**, 617–647 (2017).

[51]S. Jain, P. Tiso, and G. Haller, "Exact nonlinear model reduction for a von kármán beam: Slow-fast decomposition and spectral submanifolds," J. Sound Vib. **423**, 195–211 (2018).

[52]S. Ponsioen, T. Pedergnana, and G. Haller, "Automated computation of autonomous spectral submanifolds for nonlinear modal analysis," J. Sound Vib. **420**, 269–295 (2018).

[53]A. Vizzaccaro, A. Opreni, L. Salles, A. Frangi, and C. Touzé, "High order direct parametrisation of invariant manifolds for model order reduction of finite element structures: Application to large amplitude vibrations and uncovering of a folding point," Nonlinear Dyn. **110**, 525–571 (2022).

[54]S. Ponsioen, T. Pedergnana, and G. Haller, "Analytic prediction of isolated forced response curves from spectral submanifolds," Nonlinear Dyn. **98**, 2755–2773 (2019).

[55]M. Li and G. Haller, "Nonlinear analysis of forced mechanical systems with internal resonance using spectral submanifolds, part II: Bifurcation and quasi-periodic response," Nonlinear Dyn. **110**, 1045–1080 (2022).

[56]M. Cenedese, J. Axås, H. Yang, M. Eriten, and G. Haller, "Data-driven nonlinear model reduction to spectral submanifolds in mechanical systems," Phil. Trans. R. Soc. A. **380**, 2229 (2022).

[57]F. Mahlknecht *et al.*, "Using spectral submanifolds for nonlinear periodic control," in *2022 IEEE 61st Conference on Decision and Control (CDC)* (IEEE, 2022), pp. 6548–6555.

[58]J. I. Alora, M. Cenedese, E. Schmerling, G. Haller, and M. Pavone, "Data-driven spectral submanifold reduction for nonlinear optimal control of high-dimensional robots," arXiv:2209.05712v3 (2022).

[59]M. Li, S. Jain, and G. Haller, "Model reduction for constrained mechanical systems via spectral submanifolds," Nonlinear Dyn. **111**, 8881–8911 (2023).

[60]S. Ponsioen, S. Jain, and G. Haller, "Model reduction to spectral submanifolds and forced-response calculation in high-dimensional mechanical systems," J. Sound Vib. **488**, 115640 (2020).

[61]A. Opreni, A. Vizzaccaro, C. Touzé, and A. Frangi, "High-order direct parametrisation of invariant manifolds for model order reduction of finite element structures: Application to generic forcing terms and parametrically excited systems," Nonlinear Dyn. **111**, 5401–5447 (2022).

[62]S. Jain, T. Thurnher, M. Li, and G. Haller, see https://doi.org/10.5281/zenodo.4614201 for "SSMTool 2.4: Computation of Invariant Manifolds in High-Dimensional Mechanics Problems" (2023).

[63]G. H. Golub and C. F. V. Loan, *Matrix Computations* (Johns Hopkins University Press, 2013), see https://jhupbooks.press.jhu.edu/title/matrix-computations.

[64]J. Guckenheimer and P. Holmes, *Nonlinear Oscillations, Dynamical Systems, and Bifurcations of Vector Fields*, Applied Mathematical Sciences Vol. 42 (Springer, New York, 1983), see http://link.springer.com/10.1007/978-1-4612-1140-2.

[65]E. J. Doedel, *Lecture Notes on Numerical Analysis of Nonlinear Equations* (Springer, Dordrecht, 2007), pp. 1–49, see https://doi.org/10.1007/978-1-4020-6356-5_1.

[66]C. C. Chen and M. K. Yeh, "Parametric instability of a beam under electromagnetic excitation," J. Sound Vib. **240**, 747–764 (2001).

[67]A. H. Nayfeh, D. T. Mook, and S. Sridhar, "Nonlinear analysis of the forced response of structural elements," J. Acoust. Soc. Am. **55**, 281–291 (1974).

[68]S. S. Rao, *Vibration of Continuous Systems* (Wiley, 2006).

[69]Z. Q. Lu, J. M. Li, H. Ding, and L. Q. Chen, "Analysis and suppression of a self-excitation vibration via internal stiffness and damping nonlinearity," Adv. Mech. Eng. **9**(12), 1 (2017).

[70]S. Chatterjee, "Non-linear control of friction-induced self-excited vibration," Int. J. Non-Linear Mech. **42**, 459–469 (2007).

[71]A. Malas and S. Chatterjee, "Analysis and synthesis of modal and non-modal self-excited oscillations in a class of mechanical systems with nonlinear velocity feedback," J. Sound Vib. **334**, 296–318 (2015).

[72]H. Fu, C. Liu, Y. Liu, J. Chu, and G. Cao, "Selective photothermal self-excitation of mechanical modes of a micro-cantilever for force microscopy," Appl. Phys. Lett. **99**, 173501 (2011).

[73]J. Warminski and K. Szabelski, "The non-linear vibrations of parametrically self-excited system with two degrees of freedom," J. Theor. Appl. Mech. **33**, 643–665 (1995), see http://www.ptmts.org.pl/jtam/index.php/jtam/article/view/v33n3p643/0.

[74]G. Gobat *et al.*, "Reduced order modelling and experimental validation of a MEMS gyroscope test-structure exhibiting 1:2 internal resonance," Sci. Rep. **11**, 16390 (2021).

22 July 2024 13:58:33